Jakob Ratzenberger, BSc

Comparison between US Flow Measurement, MRI Flow Measurement and FSI Simulation of the PWV in lumen manufactured from linear elastic materials

MASTER THESIS

to achieve the university degree of

Master of Science

Master's degree programme: Biomedical Engineering

submitted to

Graz University of Technology

Supervisor

Univ.-Prof. Dipl.-Phys. Dr.rer.nat. Martin Uecker

Institute of Biomedical Imaging

Co-Supervisor

Assoc.Prof. Dipl.-Ing. Dr.techn. Gerhard Sommer

Institute of Biomechanics

Graz, March 2026

Affidavit

I declare that I have authored this thesis independently, that I have not used other than the declared sources/resources, and that I have explicitly indicated all material which has been quoted either literally or by content from the sources used. The text document uploaded to TUGRAZonline is identical to the present master's thesis.

17.03.2026

Date

Signature

Acknowledgments

I would like to take this opportunity to thank my family. Thank you for not only supporting me financially, but also for always being there to listen when things got tough and I wondered why I was putting myself through it all. Many thanks also to my girlfriend, who supports me every day, pushes me, and has my back when I've once again overloaded my schedule. Without you all, I wouldn't be the person I am today!
Furthermore, i would like to thank the entire team at the Institute of Biomedical Imaging at Graz University of Technology. It is anything but a given that you receive such support and opportunities for your master's thesis. The excellent infrastructure is one thing, but the people are even more important. Many thanks to Martin Uecker for his valuable theoretical input. Many thanks to Phillip for the countless hours you spent helping me with the MRI measurements, reconstructing the images, and solving the occasional IT problem. Thanks to Julia, Manuel, Walter, Nick, and everyone at the institute who helped me when I was once again searching for components or solutions!

Abstract

This thesis documents the development of aortic phantoms which allow the comparison of the pulse wave velocity determined by magnetic resonance flow measurements, ultrasonic flow measurements, fluid-solid interaction simulations and analytical calculations. These measurements and calculations are intended to provide a deeper understanding of how the mechanical properties of flow phantoms influence pulse wave velocity and to what extent the pulse wave velocities determined using the various methods agree with one another.

The evaluation of material options for the manufacturing process led to the conclusion that two-component silicones are the most suitable choice. Further measurements in the form of uniaxial extension tests were performed on the selected materials, and aorta phantoms were manufactured using a specifically designed mold and a standardized workflow. For the simulations conducted with svFSI from the SimVascular toolbox, the mechanical properties determined from the uniaxial extension tests were employed.
The results of uniaxial extension tests shows that the selected materials can be processed in such a way that the mechanical properties are reproducible between samples from different batches. Using the developed mold and standardized workflow, two aorta phantoms were manufactured for the flow measurements.

A comparison of the measurement methods indicates that ultrasound-based measurements, magnetic resonance measurements, and numerical simulations yield a pulse wave velocity in the same range. As expected, the pulse wave velocity was higher in the stiffer phantom than in the softer phantom. In contrast, the pulse wave velocity, calculated using the Moens–Korteweg equation, shows a noticeable deviation from these results. Consequently, additional measurements were conducted at varying pulse frequencies, revealing a pronounced dependence of pulse wave velocity on pulse frequency.

Keywords:
Pulse wave velocity, Phase Contrast MRI, Flow US, FSI-Simulation, Aorta Phantom

Contents

List of Tables

List of Figures

Unless stated otherwise in the figure caption, all figures were created by the author, Jakob Ratzenberger.

Nomenclature

v_{enc}	Velocity encoding factor
$2kSilicone$	Two component silicone
$BART$	Berkeley advanced reconstruction toolbox
CAD	Computer aided design
$DS10S$	Smooth On Inc. DragonSkin 10S
$DS20$	Smooth On Inc. DragonSkin 20
$DS30$	Smooth On Inc. DragonSkin 30
$E - modulus$	Elastic modulus
$EF00 - 30$	Smooth On Inc. Ecoflex 00-30
FDM	Fused deposition modeling
$FL300$	BASF Ultracur3D FL 300
FSI	Fluid structure interaction
$NLINV$	Nonlinear inversion
PTP	Peak-to-peak
PTT	Pulse transit time
PVC	Polyvinylchlorid
PWV	Pulse wave velocity
RF	Radio frequency
ROI	Region of interest
RPM	Rounds per minute
TE	Time to echo
ToF	Time of flight
TR	Time to repetition
UAT	Uniaxial extension test
US	Ultrasound
WK	Windkessel

1 Introduction & Theoretical background

1.1 Motivation

Cardiac diseases remain the leading cause of mortality in developed countries [1]. Studies have shown, that increased arterial stiffness, in particular of the aorta, constitute a early stage indicator of an increased risk of a variety of diseases including coronary artery disease, diabetes and renal failures [2], [3], [4]. That is why the correct determination of the stiffness has become increasingly important in recent years. In vivo, arterial stiffness is typically quantified by measuring the velocity at which the pressure pulse, generated by cardiac contraction, propagates along the arterial lumen. This velocity, referred to as the pulse wave velocity (PWV) is directly proportional to the stiffness of the arterial wall. Consequently, PWV serves as an indicator of vascular integrity and overall cardiovascular health [5], [6]. Historically, the determination of the PWV required invasive approaches due to the absence of reliable non-invasive alternatives. Only with the development of advanced diagnostic methods such as Doppler ultrasound and cardiac magnetic resonance imaging, it has been possible to assess the condition of the vessel walls non-invasively [6], [7], [8]. Nowadays, the Doppler ultrasound is considered the gold standard, although it also has some disadvantages. Local anomalies, such as those found in arteriosclerosis, can only be detected to a certain extent using ultrasound due to the limited number of acoustic windows (e.g. intercostal spaces). In addition, problems may arise when spatially classifying the flow velocity measurement using ultrasound. These problems do not arise with MRI imaging (no acoustic window required, well defined slice positions). For these reasons and due to developments in MRI imaging in general (improved scan time, increased spatial and temporal resolution) the measurement of the PWV using MRI is getting increasingly relevant. However, the measurement of the PWV using MRI is not yet sufficiently developed to be used in clinical diagnostics. For example, the accuracy of this method still needs to be investigated using measurements of flow in vessel phantoms with defined mechanical properties [9], [10].

1.2 Goal of this thesis and the research question

The objective of this thesis is to improve the understanding of how MRI-based estimations of PWV relate to the underlying physical properties of the investigated materials. In particular, this work aims to bridge the gap between the material properties of vascular flow phantoms and the corresponding PWV estimations obtained through different analytical, numerical, and experimental approaches. In the last phase, the theoretical predictions based on material parameters and fluid–structure interaction (FSI) simulations are compared with experimentally determined PWV values derived from ultrasound (US) flow measurements and phase-contrast MRI. These approaches are systematically evaluated within a unified experimental framework that enables both US and flow measurements to be performed on the same vascular flow phantom.
Accordingly, the central research question of this thesis is:
What level of agreement and systematic differences exist between pulse wave velocity values determined using US flow measurements, MRI flow measurements, analytical models, and

fluid–structure interaction simulations in aortic phantoms?
This comparative analysis aims to provide insight into the strengths and limitations of each approach for PWV determination in linearly elastic vessel phantoms.

1.3 Structure of the thesis

This thesis is structured into an Introduction Section which is giving an overview of the anatomic and biomechanical background, the definition of the PWV and the magnetic resonance imaging (MRI). In the Methods Section, the workflow from the raw materials to the mechanical tests, ultrasonic measurement and MRI measurement is outlined. In the Results Section, the outcome of these measurements and test are presented which are further discussed in the Discussion chapter. The final Chapters Conclusion and Outlook address possible improvements in further work.

1.4 Physiological and biomechanical background

1.4.1 The human heart

The human heart can be described as a periodically working pump where each cardiac cycle can be divided into the filling phase, isovolumetric contraction phase, ejection phase and isovolumetric relaxation phase [11]. The phases are separated by the opening and closing of the cardiac valves. Anatomically speaking, the heart can be divided into two halves, which can be further divided into an atrium and a ventricle [12]. The left and the right side are thereby separated by the interventricular septum (wall between the ventricles) and the interatrial septum (wall between the atrials). The atrial receive the blood from the vena cava (right atrium) and the blood from the pulmonary vein (left atrium) and the ventricles eject the blood into the pulmonary artery (right ventricle) and the aorta (left ventricle). Via the pulmonary artery, the blood flows to the lungs, where the blood is oxygenated. Via the aorta, the body gets supplied with oxygenated blood.
The anatomy of the human heart and the flow path of the deoxygenated and oxygenated blood is schematically shown in Figure 1.1.

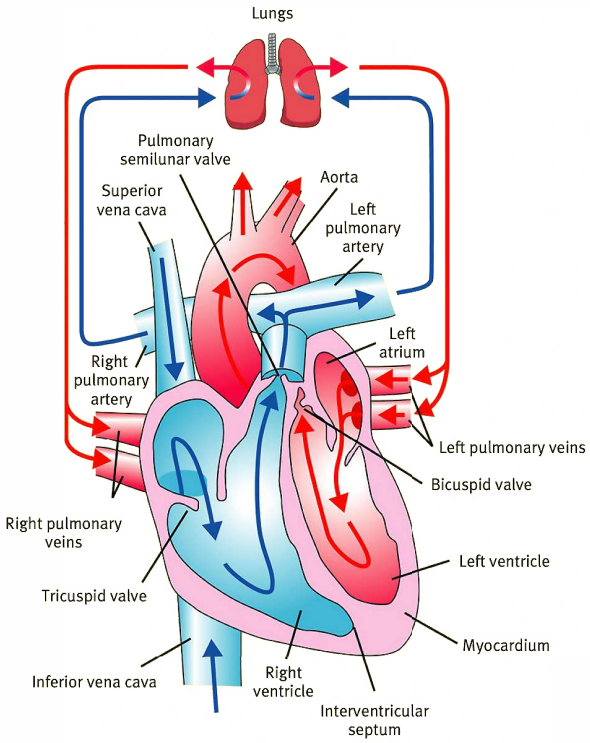

Figure 1.1: Schematic overview of the anatomy of the human heart and the flow path. Figure adapted from C. D. Fang, The cardiac cycle [11].

The way, the heart ejects the blood leads to a pulsatile blood flow in the aorta. This phenomenon was first described in 1733 by Stephen Hales. The elasticity of the aortic wall thereby leads to an expansion of the vessel [13].

1.4.2 The human aorta

The wall of the human aorta can be divided into three distinct layers which are the tunica intima, tunica media and tunica adventitia. These layers are illustrated in Figure 1.2 [14]. The tunica intima forms the inner most layer and can be further divided into the endothel and the tunica elastica interna. This layer provides a smooth and nonthrombogenic inner surface and separates the aortic wall from the blood flow.
The tunica media is the most prominent layer of the three layers and is composed of the lamina muscularis and the tunica elastica externa [15],[16]. The lamina muscularis consists of smooth muscle cells. The tunica elastica externa is formed from layered elastic tissue containing elastic fibers. Muscular and elastic components allow the aorta to expand and contract in reaction to the changing pressure during a cardiac cycle. This process is further discussed in the Section 1.4.3 .
The tunica adventitia builds the outer layer of the aortic wall and is built from collagen fibers, mast cells and fibroblasts. It supports the vessel and gives it its structure [17].

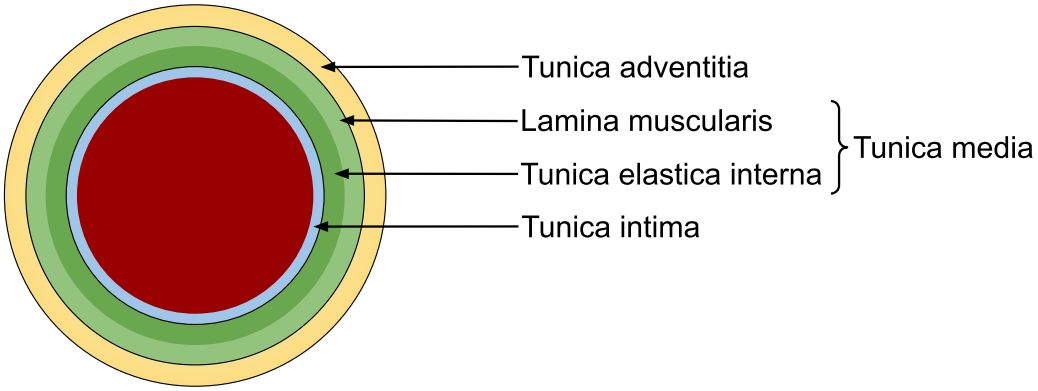

Figure 1.2: The macro anatomy of the human aorta. The aortic wall can be divided into the main layers. The tunica adventitia shown in yellow. The tunica media shown in green tones and the tunica intima shown in blue.

1.4.3 The windkessel effect

The windkessel (WK) effect describes the dampening of pressure peaks in flow systems [13]. In the human body, the heart pumps the blood in a periodic cycle. Therefore, the blood flow is not continuous, but follows the heart cycle. By the elasticity of the aorta, these pressure peaks are dampened and the amplitude of the pressure peaks is reduced. This behavior can be compared to a capacitor in an electronic circuit. The simplest approximation is the 2-element WK, consisting of a capacitor and a parallel resistor where the resistor represents the peripheral resistance. In this model, the total resistance is highly frequency dependent and drops for high frequencies to a negligibility low value. Therefore, the characteristic impedance of the aorta was added to the model leading to the 3-element WK. In order to further reduce the error at low frequencies, the 4-element WK model was developed. For this model of the WK effect, an inertance was added parallel to the impedance. This represents the inertia of the lungs and thorax. The added inertance is difficult to determine in practice, which is why the 3-element WK is still used to today to model the WK effect. With the 3-element WK, the relationship between the prevailing pressure and the resulting flow can be adequately modeled using a few physiological parameters. However, the WK model also has limitations. Limitations are for example wave transmission and wave motion in the aorta and thus also the pulse wave velocity can not be modeled with this model [13].

1.5 Pulse wave velocity

With the opening of the aortic valve in the beginning of the ejection phase and the ejection of the stroke volume into the ascending aorta, a pressure wave is created in the aorta. This wave propagates along the vessel with a distinct speed refereed as the PWV usually measured in $m \cdot s^{-1}$ [18], [19].

The PWV is dependent on a number of factors. One key factor is the elasticity of the blood vessel in which the wave propagates [18]. Essentially, the PWV is higher in a rigid vessel than in an elastic vessel with the same geometry and fluid density. This is why the PWV velocity became an important indicator for atherosclerosis and determinant for anti-hypertensive treatment [20], [21]. This issue is discussed in more detail in chapter 1.6.3.

1.5.1 Measurement of the PWV

As discussed in Section 1.5, the

$$PWV = \frac{x}{\Delta t} \tag{1}$$

describes the time Δt it takes a pressure wave to travel a certain distance x along a lumen with an elastic wall.
So to measure the PWV, the time it takes the wave to travel the set distance between two measuring points must be determined.
To measure the time offset of the wave, various approaches can be applied [8], [22]. The main methods used in literature are the time-to-foot, time-to-peak, time-to-upslope and the cross correlation method. The time-to-foot approach uses the time shift between the flow minima. The time-to-peak approach in contrast uses the shift of the flow peaks (flow maxima). For the time-to-upslope approach a line is drawn through 20% and 80% of the respective maximum and the time shift of these lines is used. The cross-correlation method evaluates the similarity between the inflow and the outflow by systematically shifting one signal relative to the other in time. The time delay between the signals is determined by identifying the shift at which the similarity, quantified by the cross-correlation function, reaches its maximum.

1.6 Biomechanics

1.6.1 Elastic modulus

The strain a material experiences in reaction to an applied one dimensional force is defined as the elastic modulus (E-modulus), also called elasticity modulus or Young's modulus [23]. Mathematically, the elastic modulus is defined as

$$E = \frac{\sigma}{\epsilon} = \frac{F/A}{\Delta L/L_0} = \frac{F \cdot L_0}{A \cdot \Delta L} \tag{2}$$

where σ

$$\sigma = \frac{F}{A} \tag{3}$$

represents the stress, defined as force F per unit area A and ϵ

$$\epsilon = \frac{\Delta L}{L_0} \tag{4}$$

the change in length ΔL relative to the initial length L_0 represents. E is therefore given in force N per area. The area is often given in square millimeter since

$$1 \ \frac{\mathrm{N}}{\mathrm{mm}^2} = 1 \ \mathrm{MPa}. \tag{5}$$

Although an artery is a three dimensional structure, the main deformation occurs in the radial direction. The deformations in the circumferential and longitudinal direction play thereby a secondary role [23].

1.6.2 Poisson's ratio

The Poisson's ratio describes the ratio of transversal strain to axial strain in reaction to an unidirectional, external force. In the past, a number of different definitions for the ratio where introduced, but two definitions dominate the literature. The incremental approach and the definition through logarithmic strains.
For this project, the definition of the Poisson's ratio as the ratio between the lateral strain and the longitudinal strain

$$v_{poission} = -\frac{\epsilon_{lat}}{\epsilon_{long}} \tag{6}$$

is used [24].

1.6.3 Moens-Korteweg equation

As discussed prior, the PWV is among other things, dependent on the elasticity of the blood vessel. To derive the PWV for a given vessel geometry and given elastic modulus the Moens-Korteweg equation was derived by Moens, A. Isebree and D. J. Korteweg independently in the year 1877 [25], [26]. The derived equation is valid for the wave propagation in axial symmetric, rubber and intestine tubes with isotropic wall materials and incompressible fluid. In addition, the formula is only valid for linear wave propagation and does not take reflections into account [27], [28].

$$c_{\text{moens}} = \sqrt{\frac{Eh}{2R\rho}} \tag{7}$$

Where E represents the E-modulus, h the wall thickness of the vessel, R the inner diameter of the vessel and ρ the density of the fluid. In its original form, the Moens-Korteweg equation assumes a thin-walled vessel, simplifying the relationship between the wave speed and the wall thickness.
The modified Moens-Korteweg equation

$$c_{\text{moens,modified}} = \sqrt{\frac{Eh}{2R\rho(1 - v_{poission}^2)}} \tag{8}$$

takes the wall thickness into account by including the Poisson's ration v into the formula [28].

1.7 MRI flow measurement

Magnetic resonance imaging (MRI) makes use of the phenomenon of the intrinsic angular momentum of 1H atoms, also known as spin, and excite these spins with the aid of high-frequency pulses in order to obtain a signal that can be measured in receiver coils [29], [30].

1.7.1 Spin

The nuclei of hydrogen atoms (1H atoms) possess a so-called nuclear spin, also known as intrinsic angular momentum, in addition to their high mass and positive electrical charge compared to electrons. The combination of the positive electric charge and the intrinsic angular momentum leads to moving charges. This causes a magnetic field with a dipole characteristic, whereby the axis of symmetry is oriented along the axis of rotation of the nucleus. The frequency of the spin is called the Larmor frequency and depends on the strong external magnetic field B0 [29], [30].

1.7.2 B0 field

If a static magnetic field B0 is introduced from outside, the axis of symmetry of the magnetic field and thus also the axis of rotation of the nucleus is aligned along this field.
If not a single atom is considered, but a body consisting largely of 1H atoms, it can be seen that a number of nuclei are aligned along this B0 field depending on the strength of the external magnetic field. In the case of a B0 field with a field strength of 3 Tesla, approximately 1/100000 or 0.01% nuclei align along it. This state is called the equilibrium state M0 [29], [30].

1.7.3 High-frequency pulse

These spins can be deflected from the equilibrium state into an excited state with a impulse. The longitudinal magnetization is converted into a transverse magnetization. This excitation happens by applying a radio frequency (RF) transmitter with a frequency close to the Larmor frequency. As already mentioned, the Larmor frequency depends on the strength of the external magnetic field and is 127.8 MHz for a 3 Tesla B0 field. The magnetization vector of the deflected nuclei can be broken down into two components, the longitudinal magnetization M_z and the transverse magnetization M_{xy}, whereby only the transverse magnetization in receiver coils contributes to a measurable signal. The degree of deflection, also known as the flip angle, can be determined with the length of the RF pulse and can assume values between 0° (=no deflection) and 180° (=magnetization vector points in the opposite direction of the B0 field).
These high-frequency pulses introduce energy into the patient and can cause the patient to heat up. The energy transferred to the patient is measured in watts per kilogram and is referred to as the Specific Absorption Rate [29], [30].

1.7.4 Relaxation

Following such a deflection, the magnetization vector of the atom strives to return to the equilibrium state M0.
This process, also known as relaxation, can be described with the time constants T1 and T2, where T1 indicates the time duration of the RF pulse in which M_z is still 37% of the equilibrium state M0 [29], [30].

1.7.5 Trajectory

As explained above, the frequency of the nuclear spin and thus also the frequency required to excite the spin, depends on the external magnetic field. If, in addition to the B0 field, a magnetic field is introduced that increases along a direction in space, the spins along this direction have a Larmor frequency that depends on their position along that gradient. These additional magnetic fields, also called gradient fields, superimpose the B0 field and are generated by gradient coils.
To capture a MRI image, the effect of this gradient on the frequency and phase of the spins is exploited and the signals received in receiver coils are stored in a raw data space also known as k-space.
The received signal depends on the direction and length of the sum vector of the transverse magnetization. The k-space represents a matrix, with the phase encoding plotted on the y-axis and the frequency encoding on the x-axis. The phase gradient determines the beginning point of the k-space line and the frequency gradient then fills this line. The time span between the middle of the excitation by the RF pulse and the middle of the readout gradient is called the time to echo (TE).
The time to repetition (TR) describes the time span between two consecutive RF pulses. The time required to fill the k-space is calculated from the number of lines in the k-space multiplied by the TR [29], [30].
Switching on only one gradient at a given time the k-space is filled line by line (=horizontal k-space lines, see Figure 1.3 (a)). This is referred to as a Cartesian trajectory.
Switching on two or more gradients simultaneously leads to a superposition of the B0 field, the first gradient and the second gradient. This allows the k-space to be filled with data along a configurable trajectory. An example of such a non-Cartesian sequence is filling the k-space with a radial sequence. In this case, all spokes run through the center of the k-space as shown in the Figure 1.3 (b) [29].

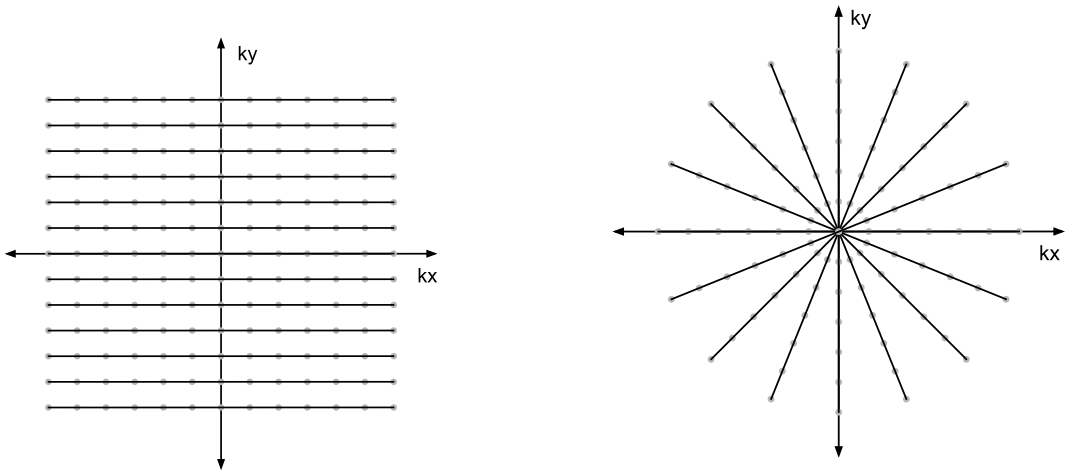

(a) (b)

Figure 1.3: (a) Using a Cartesian trajectory the k-space is filled line by line, resulting in a grid. (b) In a radial sequence, the trajectories go through the center of the k-space.

The angle between the spokes in a radial sequence is important in this regard. By selecting a so called golden angle and adjusting the number of spokes accordingly, it is possible to achieve good coverage of the k-space with fewer spokes. This allows for a reduction in the number of spokes required for an usable image and consequently the time needed for a measurement [31].

Based on the golden angle, the tiny golden angle can be calculated using the formula (9).

$$\psi_N = \frac{\pi}{\tau + N - 1} \tag{9}$$

Where N represents the golden index and τ the golden ratio defined as in formula (10).

$$\tau = \frac{1 + \sqrt{5}}{2} \tag{10}$$

Numerical simulations have shown that tiny golden angles provide a good efficiency if $2N + 1$ spokes are used in the reconstruction. By applying a tiny golden angle the number of required spokes and thereby the measurement time can be reduced [32].

1.7.6 Interleaved sequence

Another approach to comparing the temporal curve of the flow in two layers is to measure the flow curve in the two layers simultaneously with an interleaved sequence. In this approach, the slice in which a spoke is captured is alternated until the desired number of spokes is captured. This procedure is visualized in the Figure 1.4.

- 1. spoke in the inflow slice
- 1. spoke in the outflow slice
- ...
- 350. spoke in the inflow slice
- 350. spoke in the outflow slice

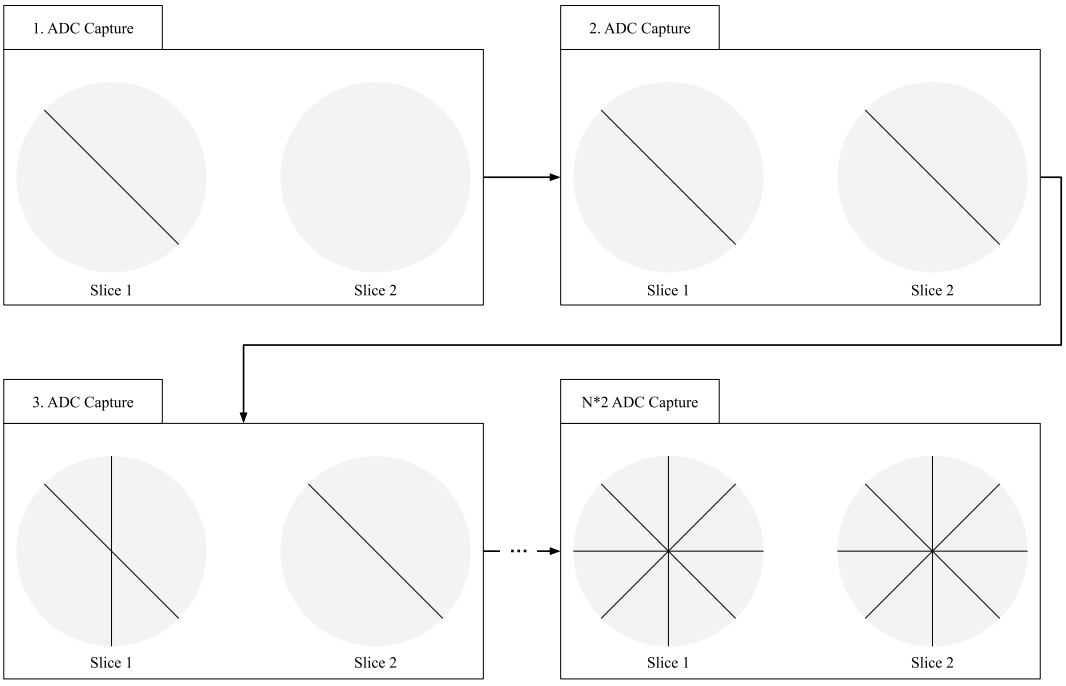

Figure 1.4: Procedure for an interleaved radial MRI sequence for two slices (S1 & S2). The spokes are captured in an interleaved way which leads to the slices being recorded practically simultaneously.

One benefit of radial sequences is that when choosing the correct angle between the spokes (golden angle), one can acquire a large number of spokes and then later during the reconstruction define the number spokes per frame. Thereby, a large number of spokes can be transferred into a time series of images.

1.7.7 Phase contrast MRI

Two spins that experience the same magnetic field for the same time period are in phase with another because they oscillate with the same frequency (see Larmor frequency in Section 1.7.3). In turn, if one spin is in the magnetic field shorter or experiences a weaker magnetic field, the spins are out of phase. This phenomenon is used in the phase contrast (PC) MRI sequence to measure the flow of liquids. By applying a bipolar gradient (gradient G1 and G2 in the Figure 1.5) along the same axis as the flow, the residual phase of a stationary spins is zero since the effect on the phase from the first gradient is canceled out by the second gradient. The moving spins on the contrary change their position and therefore the second gradient does not cancel out the effect of the first gradient. This results in a residual phase which is proportional to the velocity of the spins. To compensate the local susceptibility differences, this is repeated with an inverted bipolar gradient (gradient G3 and G4 the Figure 1.5).

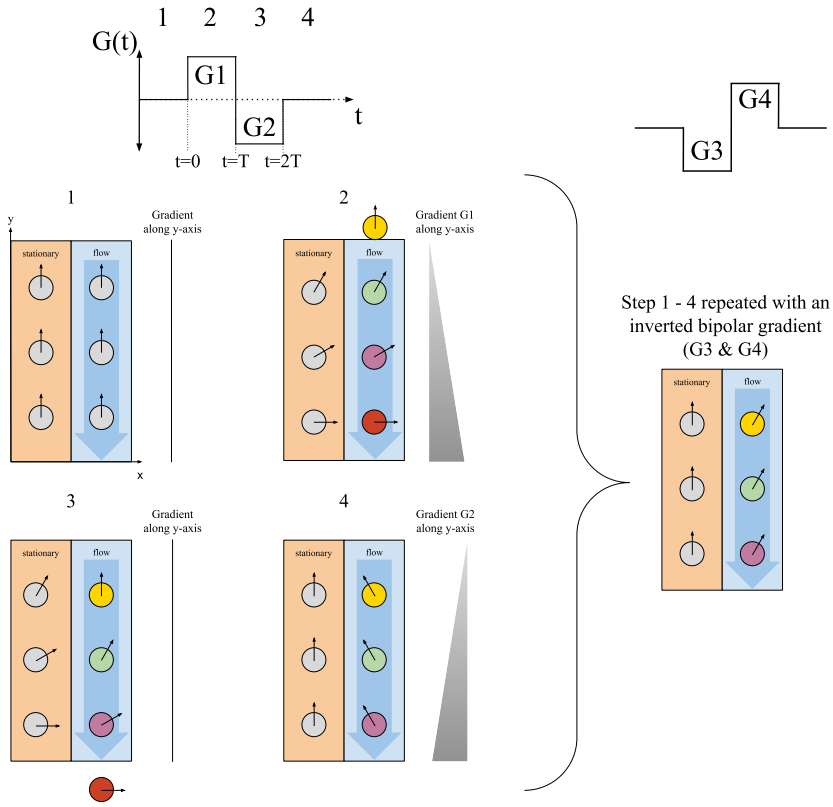

Figure 1.5: A phase contrast MRI sequence can be divided in four phases which are repeated with an inverted bipolar gradient to compensate local susceptibility differences. To receive the final phase contrast image the phase difference between the first image (bipolar gradient) and the second image (inverted bipolar) is calculated.

The PC phenomenon can also be expressed by formulas.
The phase accumulation is defined as following:

$$\begin{aligned}\Delta\phi(t) &= \gamma \int_{t_0}^{t} \vec{r}(\tau) \cdot \vec{G}(\tau) d\tau \\ &= ... = \gamma(\vec{r}_0 \cdot \vec{m}_0 + \vec{v} \cdot m_1 + ...)\end{aligned} \tag{11}$$

where $\vec{m}_i$ represents the gradient moment

$$\vec{m}_i := \int_{t_0}^{t} (\tau - t_0)^i \vec{G}(\tau) d\tau \tag{12}$$

and τ the observation time. $\vec{G(\tau)}$ represents the gradient and γ the gyromagnetic ratio.
Assuming a constant speed and constant gradients, the phase accumulation simplifies to

$$\Delta\phi_1(t) = \gamma(t\vec{r}_0 + \frac{1}{2}t^2\vec{v}) \cdot \vec{G} \tag{13}$$

$$\Delta\phi_1(T) = \gamma(T\vec{r}_0 + \frac{1}{2}T^2\vec{v}) \cdot \vec{G} \tag{14}$$

for the positive gradient from $t_0 = 0$ to T and $\vec{r}(t_0) = \vec{r}_0$.
For the negative gradient, the phase accumulation is correspondingly

$$\Delta\phi_2(t) = -\gamma(t - T)(\vec{r}_0 + T\vec{v}) \cdot \vec{G} - \gamma\frac{1}{2}(t^2 - T^2)\vec{v} \cdot \vec{G} \tag{15}$$

$$\Delta\phi_2(2T) = \gamma(T\vec{r}_0 + T^2\vec{v} + \frac{3}{2}T^2\vec{v}) \cdot \vec{G} \tag{16}$$

for the positive gradient from T to $2T$ and $\vec{r}(T) = \vec{r}_0 + T\vec{v}$.
Combining the positive and the negative Gradient the residual phase can be described by

$$\begin{aligned}\Delta\phi_1(T) + \phi_2(2T) &= \gamma(\frac{1}{2}T^2\vec{v} - \frac{3}{2}T^2\vec{v}) \\ &= -\gamma T^2\vec{v} \cdot \vec{G}\end{aligned} \tag{17}$$

The phase of the spins can be converted using the velocity encoding factor (v_{enc}). This factor can be calculated using the formula

$$v_{\text{enc}} = \frac{\pi}{\gamma \cdot |\Delta m|} \tag{18}$$

where γ represents the gyromagnetic ratio and $|m|$ the change at the beginning of the bipolar gradient. The v_{enc} is given in $\frac{cm}{s}$.
So the flow velocity is given by

$$v = \frac{\Delta\phi}{\pi} \cdot v_{enc} \tag{19}$$

in $\frac{cm}{s}$ where ϕ is the phase of the moving spins. When the flow velocity is underestimated and a v_{enc} is chosen that is too low, phase wrapping occurs. This results in a incorrect interpretation of the phase and a flow in the opposite direction [33].

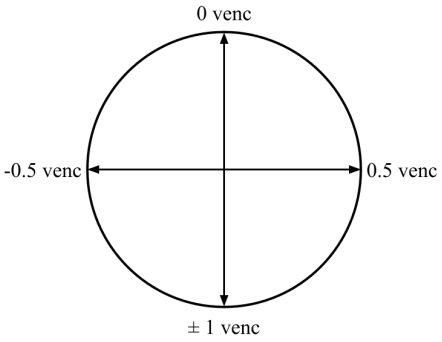

Figure 1.6: The residual phase is translated to the flow velocity using the v_{enc}. One π of phase shift corresponds to a flow velocity of one v_{enc}.

The time per frame for a normal radial phase contrast sequence can then be calculated via the following formula with TE as the time to echo and N_{spokes} being the number of spokes used per image. The multiplication factor 2 comes from the reference image needed for the phase contrast imaging (see 1.7.7). This leads to a frame time of

$$T_{perFrame} = TE \cdot N_{spokes} \cdot 2 \tag{20}$$

When using a interleaved radial phase contrast sequence, the frame time is twice as big since two slices are measured simultaneously.

$$T_{perFrame} = TE \cdot N_{spokes} \cdot 2 \cdot 2 \tag{21}$$

2 Methods

To answer the research question defined in 1.1, preliminary work must be carried out in order to perform the MRI and US measurements as well as the simulation and analytical calculations. In order to be able to carry out the MRI and US measurements, an aortic phantom with mechanical properties resembling those of the human aorta has to be manufactured. For the simulation and the analytical calculations, the mechanical properties of the, for the aortic phantom selected materials, must be determined. This is done by performing uniaxial extension tests.
To ensure a systematic approach, a workflow was developed to manufacture aorta phantoms from elastic materials for PWV measurements using US flow measurements and MRI PC measurement.
This workflow can be split up into multiple tasks which are shown in the Figure 2.1. For the simulation and the analytical calculation, the exact material properties of the chosen material have to be determined. To be able to perform MRI and US measurements, a robust and watertight phantom and a support structure has to be produced.

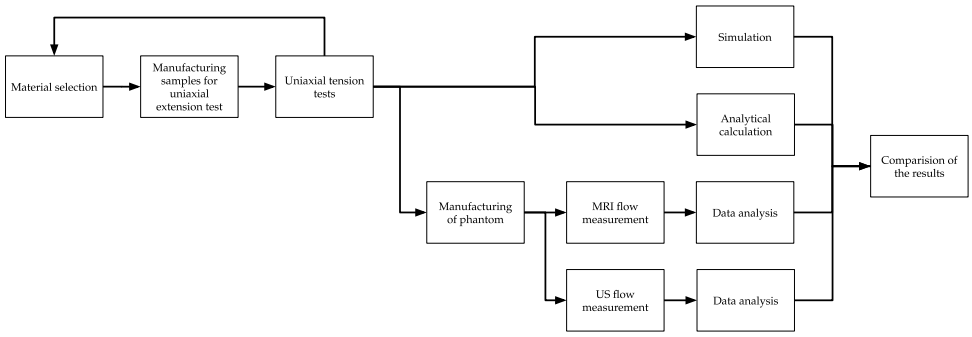

Figure 2.1: Overview of the workflow for the individual materials. Starting with the material selection and mechanical testing. The flow measurements, FSI Simulation and analytical calculation in the center and the comparison of the results in the end.

The following chapters describe all the steps that were necessary to achieve the objectives.

2.1 Material selection

Models of blood vessels for studying fluid flow can come from various sources. A basic distinction can be made between biological samples and artificial samples.
Biological samples can originate from animals or from human body donors. In order to use these for experiments, various guidelines must be followed to comply with ethical and safety requirements. In addition, the collection, storage and preparation of samples is complex and expensive. Furthermore, external influences can lead to changes or falsification of the results (drying out, cell damage, etc.) [34], [35].
Therefore, this master thesis focuses on the use of phantoms manufactured from synthetic

materials i.e., materials that have been chemically produced and are not from natural origin. Three different material categories were considered for this thesis to be potentially suitable for the manufacturing of aorta phantoms with mechanical properties similar to those of the human aorta in terms of elasticity.

- 3D printing of samples from Stratasys Tissue Matrix on a Stratasys Anatomy printer by an external company
- Self-produced 3D samples from flexible resin from a LCD resin printer
- Self-produced models from two compound silicone (2k-silicone)

2.1.1 Stratasys tissue matrix

Stratasys is a leading company in the field of 3D printing and also offers 3D anatomical prints. For this purpose, the company has a range of materials that can be processed on Polyjet printers and can produce complex geometries with a wide range of elasticities including elasticity similar to that of the human aorta [36]. For the model used in this thesis, the material "Structural Heart-Vessel Wall" from the material group "tissue matrix" was printed on an Stratasys J750 printer at the company Addion GmbH which is based in Tyrol. [37]

The model was printed twice in two different print orientations. One horizontally and one at an angle of 45 degrees in the transversal axis. Due to the high price of the material, no samples for the materials tests were ordered. Instead, the flow tests were carried out first and afterwards, the samples for the material tests were cut out of the phantom.

2.1.2 Elastic resin

The models manufactured from elastic resin were printed in house on an LD-002R printer from Creality [38]. This is an entry level LCD resin 3D printer with a build volume of 119x65x160 mm. For the phantom material, the flexible resin Ultracur3D FL 300 (FL300) from BASF was selected due to its high elasticity, robustness and compatibility with the available printer [39].

2.1.3 2k-silicone

2k-silicone was chosen as a material due to the wide range of products with varying degrees of elasticity. Furthermore, 2k-silicone also has the advantage that complex geometries can be produced relatively easily and inexpensively. In addition, 2k-silicone has proven to be potentially suitable for the manufacturing of aorta phantoms [40]. Four different 2k-silicone where chosen for further testing. These are listed in the Table 1.

Table 1: Overview of the chosen 2k-silicones.

Material	**Manufacturer**	**Abbreviation**	**E-module [kPa] (Datasheet)**
EcoFlex 00-30	Smooth On, Inc. Inc.	EF00-30	70
DragonSkin 10S	Smooth On, Inc. Inc.	DS10S	152
DragonSkin 20	Smooth On, Inc. Inc.	DS20	338
DragonSkin 30	Smooth On, Inc. Inc.	DS30	593

The recommended processing of the materials is listed in the corresponding data sheets [41], [42].

2.2 Uniaxial extension test

The uniaxial extension test (UAT) were performed in the laboratory of the Institute of Biomechanics at the Technical University Graz using a Zwick Roell Messphysik UAT with the Zwick Roell Xforce HP load cell (nominal force of 20N). This setup is shown in Figure 2.2.

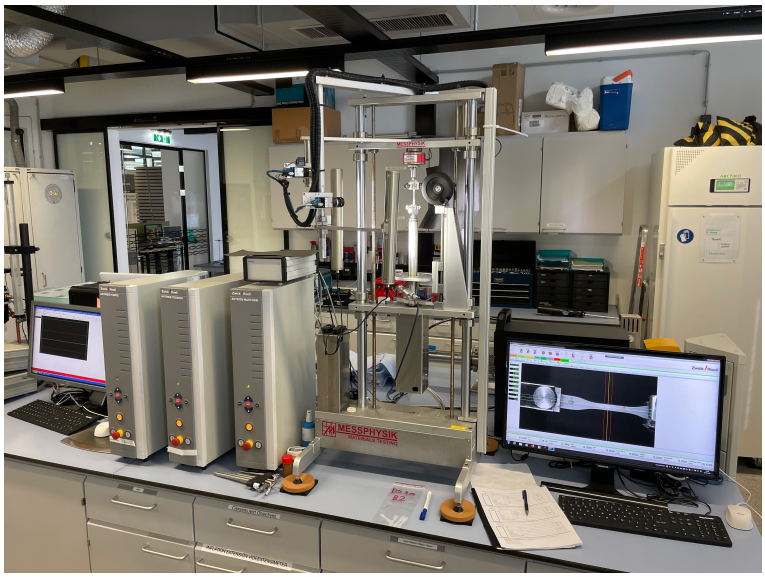

Figure 2.2: Overview of the Zwick Roell Messphysik UAT setup. On the left side are three drivers, on top of the right driver is the camera controller, in the middle is the UAT test bench with the camera, lights, load cell and the sample held by the sample holder and on the right is the computer with the monitor and the control software.

2.2.1 Manufacturing of the 2k-silicone samples

In preparation for the UATs, samples that can be clamped into the UAT setup, must be manufactured. These samples must have a specified dogbone geometry with the dimensions specified in the Figure 2.3. For the dogbone model, a two piece mold is designed. The mixed 2k-silicone is injected into the mold via a separate injection tunnel. In a single molding process, a batch of five dogbones is manufactured simultaneously. A rendering of the mold is shown in Figure 2.4.
The mold was 3D printed using an Ultimaker S5 Fused Deposition Modeling (FDM) 3D printer and black Ultimaker tough Polylactid filament.
For the design of this mold and all further models, Autodesk, Inc. Fusion 360 was used as the Computer aided design (CAD) software [43].
To allow an easier removal of the samples, the inside of the mold was coated using the A-Chem Trennspray SG-1008S mold release spray. The two halves were assembled using 4 M3 heat inserts, 4 M3 bolts and 4 M3 spacers. The .stl and .f3d file of the sample mold can be found in the Appendix [A].

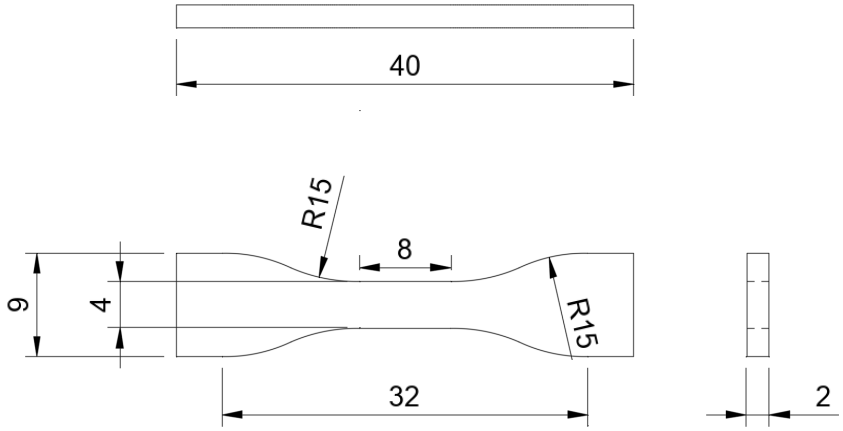

Figure 2.3: For the UATs, samples in the form of dogbones with the geometry and dimensions shown were created. All measurements in this figure are in mm.

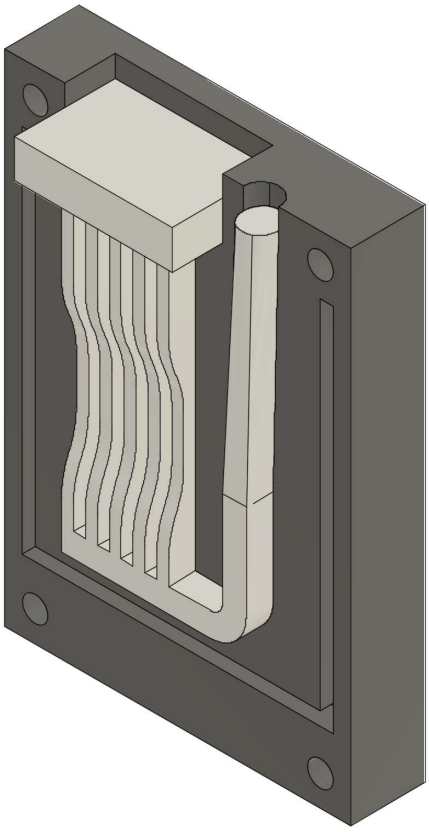

Figure 2.4: The 3D printed mold is displayed in dark grey and the five 2k-silicone samples in white. The injection tunnel is also represented in white to the right of the samples.

Whenever handling hardener or not cross-linked silicone, the safety precautions such as wearing personal protective equipment (eye protection, nitrile gloves and long-sleeved clothing) must be observed. During the handling of the silicone, care must be taken that no gloves or other objects made out of latex are used as latex can influence or prevent the correct cross-linking of the silicone. Furthermore, the whole process of preparing and injecting the silicone has to be within the drip time given by the manufacturer [41], [42].

The needed amount of 2k-silicone results from the volume of final silicon part (five UAT samples, silicone in the injection tunnel and spill over to remove air bubbles), which is approximately 10 cm^3 and the silicon that remains in the mixing container and the syringe which is approximately 5 cm^3.
The hardener and the silicone were mixed according to the manufacturer's instructions in a mixing container using a wooden spatula. To remove any air bubbles that have formed during the mixing process, the silicone was filled into a 30 ml syringe, which nozzel was caped of. This syringe was then placed in a vacuum chamber without the piston and a vacuum with -0.3 Bar was created and held for 3 minutes [44].

After the vacuum has been released by opening the air inlet of the vacuum chamber, the

plunger was placed on the syringe and the silicone was injected into the mold.
When the silicon was fully cross-linked (approximately after 12 h) the mold can be opened by loosening the M3 bolts, the silicone samples can be removed and the individual samples can be separated using a angle cutter and a scalpel.
The samples are marked right after the demolding with the sample number and the batch number using a water resistant marker to prevent mixing up the samples.

2.2.2 Preparation of the 3D printed resin samples

The resin dogbones for testing the flexible resin can be directly 3D printed using the LCD Resin printer Creality LD-002R [38].

2.2.3 Fixation of the samples

The prepared samples are fixated with two clamps as shown in the Figure 2.5. During the fixation process, the sample should not be compromised, but at the same time, the risk of the sample slipping out of the clamps must be reduced to a minimum by slowly tightening the clamps under constant monitoring. Any samples that are damaged during demolding or clamping must be sorted out.

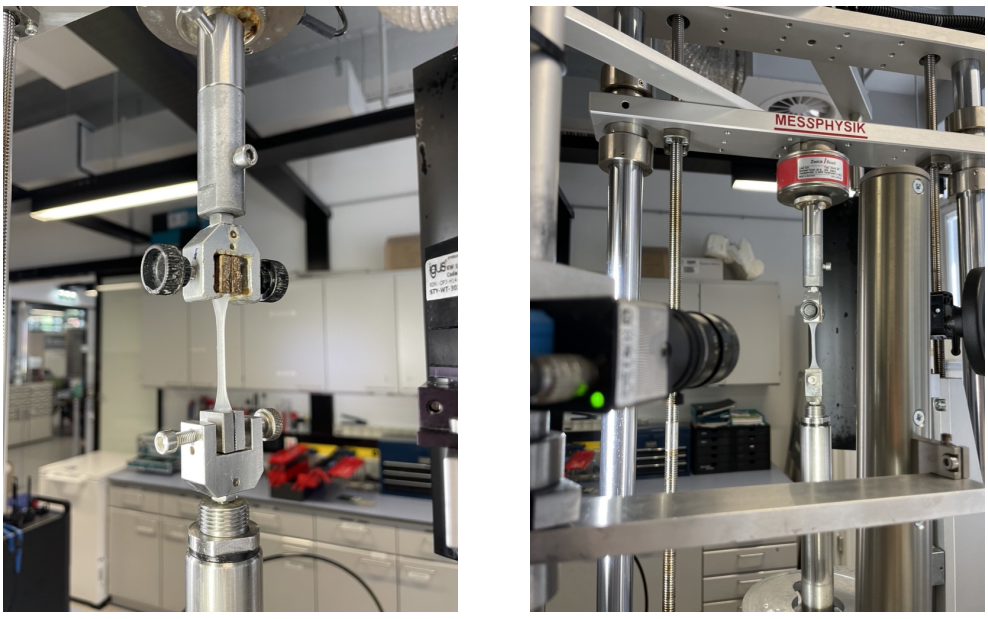

(a) (b)

Figure 2.5: (a) Clamping of the white 2k-silicone UAT sample and (b) close-up of the UAT setup (camera on the left side, in red the measurement cell and the clamped silicone sample).

2.2.4 Test protocol

For each sample, a test protocol containing

- the material,
- test date,
- individual sample ID (MaterialID_BatchNumber_SampleNumber),
- the sample dimensions,
- the cycles,
- the pull speed,
- the maximum force and
- the name of the excel sheet in which the data is stored in,

was filled out. The test protocol can be found in the Appendix [B.1].

The first step in measuring a sample was to determine its thickness using a designated image-based thickness measurement setup. Then, the sample was placed in the sample holders of the UAT test bench. Thereby it is important to ensure that the sample is not twisted and clamped perpendicular to the camera.
The initial width and initial length are then measured using the camera of the UAT setup. This is shown in Figure 2.6.

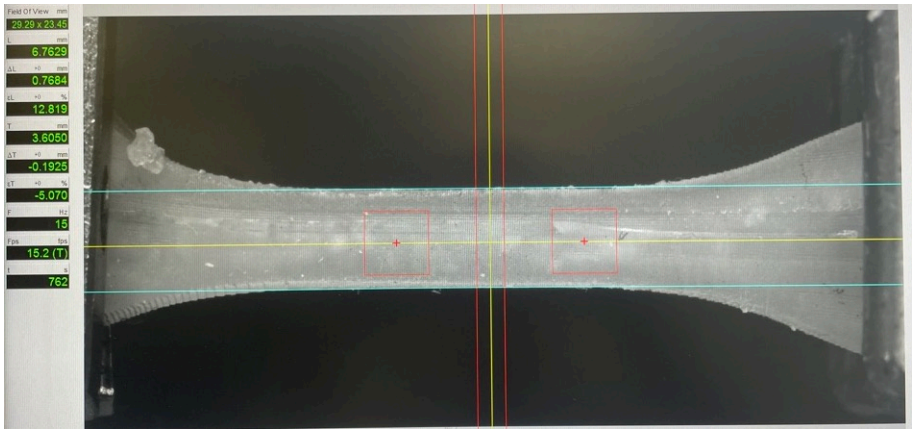

Figure 2.6: The sample (white) is automatically detected and its dimensions are measured by the UAT control software. The distance between the cyan lines corresponds to the initial width of the sample and the distance between the red crosses corresponds to the initial length. During the elongation of the sample these two parameters are measured and saved to the data file.

The elongation of the sample is controlled in the control software. The user has to define the speed and the maximum force measured in the load cell or the maximum elongation of

the sample. The following protocol was used for all samples measured in the course of this thesis:

1) Three precondition cycles from 0 to 0.6 N with 20 mm per minute

2) One pull from 0 to 5 N with 20 mm per minute

2.2.5 Data analysis

The UAT-Setup saves the time stamp, the force measured by the load cell, the longitudinal deformation and the lateral deformation in an excel sheet. A self written python program written specifically for this purpose was used for data analysis and the calculation of the mechanical properties. The data is read in and the force valleys (start pulling) and the force peaks (stop pulling) are extracted using the scipy find_peaks. Then the data points between the last pull (data between last valley and the last peak) was extracted. From this data, the stress strain curve was calculated and a linear regression was fitted. The slope of this linear regression represents the E-modulus of the material. From the longitudinal deformation and lateral deformation, the Poisson‘s ratio was calculated. This was done for all samples and then averaged for all samples of a material to get the mean E-modulus and the mean Poisson‘s ratio.
With these results and the geometry of the aorta phantom, the PWV of the material was calculated using the modified Moens-Korteweg equation (8). The algorithm for the data analysis is visualized in Figure 2.7 and can be found in the Appendix [C.2].

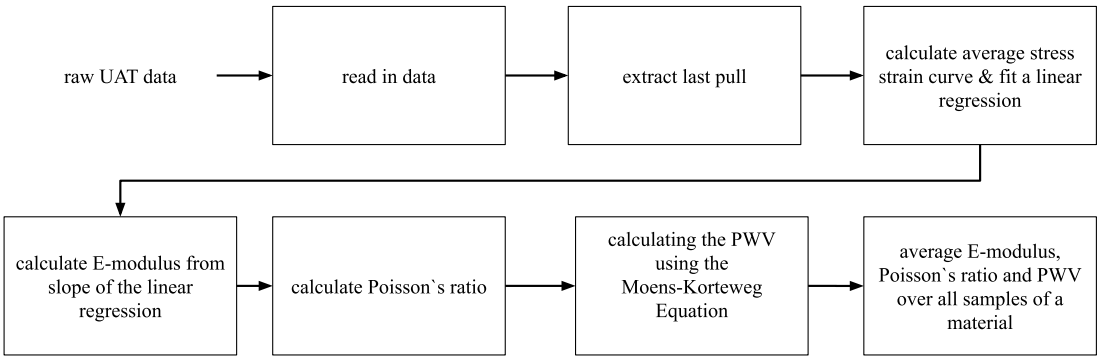

Figure 2.7: The data analysis of the raw UAT data is shown in the flow diagram above. Starting with the raw data saved by the UAT setup and ending with the extruded E-modulus and Poisson‘s ratio for the given material. To determine the reproducibility, the standard deviation between the different samples and batches was calculated.

2.3 Phantom construction

The dimensions for the phantom are chosen to roughly represent the diameter and wall thickness of the human thoracic aorta:

- 300 mm in length
- 30 mm inner diameter
- 2 mm wall thickness

These dimensions were determined in agreement with the Institute for Biomechanics at the Technical University Graz.

2.3.1 Elastic resin phantom

Since the length of the phantom exceeds the build volume of the resin 3D printer, the phantom was split into two parts. Those two parts where printed separately and then glued together using the same resin as for the parts. Afterwards, the prints were cleaned using pure isopropanol and cured using a UV chamber.

2.3.2 2k-silicone phantom

Silicone mold

The designed mold for the aortic phantom consists of four parts for the outer shell and one tube for the inner shell. A bottom bracket, a top bracket and a ring holds the parts of the outer shell in place while injecting the silicone. The assembled mold is shown in Figure 2.8.

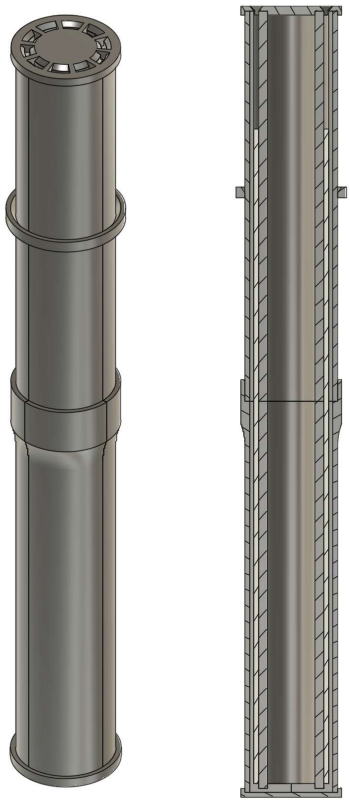

(a) (b)

Figure 2.8: (a) Rendering of the assembled phantom mold (b) cutting analysis of the mold where the 3D printed mold is shown in dark grey and the silicon phantom in white.

The .stl and .f3d file of the mold can be found in the Appendix [A].

Phantom manufacturing

Similar as for the UAT silicone samples, the inside of the mold was coated with the mold release spray. To reduce the spillage to a minimum, the assembled mold was wrapped in adhesive tape to cover up the seams of the outer shell. The procedure of injection molding the silicone is similar to the injection procedure for the UAT samples described in chapter 2.2.1. The amount of silicone needed is approximately 70 cm^3 (61 cm^3 for the phantom and 9 cm^3 to account for the silicone that remains in the container and the syringe). After mixing the silicone, it is filled into two 100 ml syringes to prevent boiling over in the vacuum chamber. When changing from the first syringe to the second one during the injection, it is essential to ensure that no air bubbles enter the mold.
The .stl and .f3d file of the phantom can be found in the Appendix [A].

2.4 Flow measurement

2.4.1 Setup

To measure the flow through the aorta phantom, a setup consisting of five main components was developed:

- water reservoir
- pump
- connection hose
- aorta phantom & support structure
- US Flow measurement.

The setup can be divided into two main parts. On the one side, there was the part of the setup that was brought into the scanner room and on the other side there was the part that must remain outside the scanner room in the control room since it is not MRI save. This is visualized in the Figure 2.9.

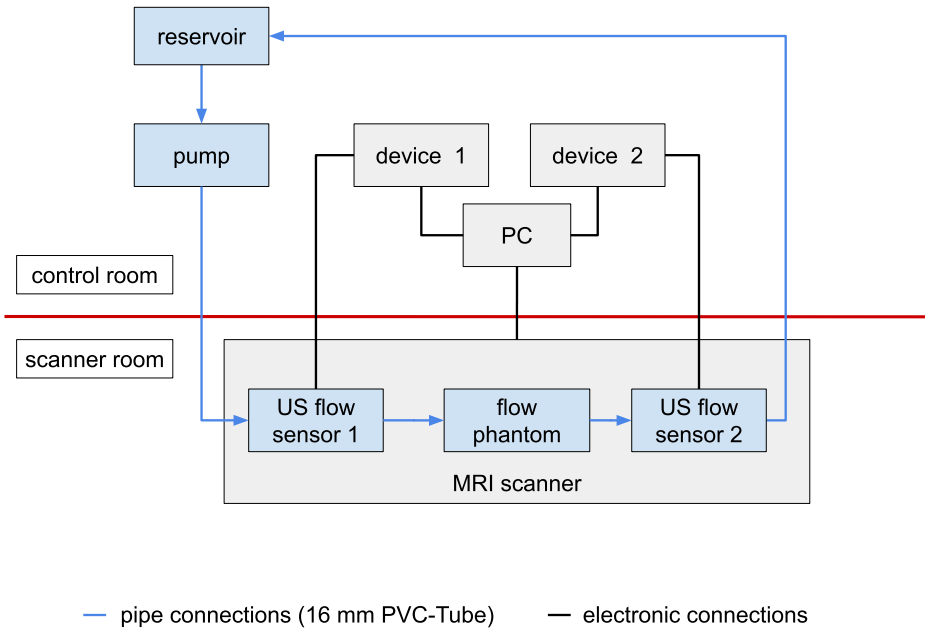

Figure 2.9: The measurement setup for the flow measurements in the MRI scanner can be divided into two main groups. The reservoir, the pump, the US devices and the PC are placed in the control room of the scanner. The US sensors and the flow phantom are placed directly in the bore of the scanner.

For the water reservoir, a barrel with a capacity of 60 liter was chosen. As for the pump, the GAMPT Multi-Flow centrifugal pump (Figure 2.10) was used.

Figure 2.10: For pumping the fluid through the setup, the GAMPT Multi-Flow in the mode 2 (negative ramp) was used.

This pump has five different modes that can be used to control the output.

0) Continuous flow rounds per minute (RPM) controlled
1) Continuous flow volume (in l/min) controlled
2) Pulsatile flow sawtooth with a negative ramp
3) Pulsatile flow triangular signal (rectified)
4) Pulsatile flow sawtooth with a positive ramp [45]

For all measurements, the mode 2 (pulsatile flow sawtooth with a negative ramp, see Figure 2.11) was used because this waveform represents best the flow in the aorta [13]. The period duration and the maximum rounds per minute can be adjusted on the pump using the control knobs [45]. For the majority of the measurements, a period duration of 1 second

was used. To investigate the dependence of the measured PWV on the period duration, the duration was increased from 500 ms to 1200 ms in 100 ms increments.

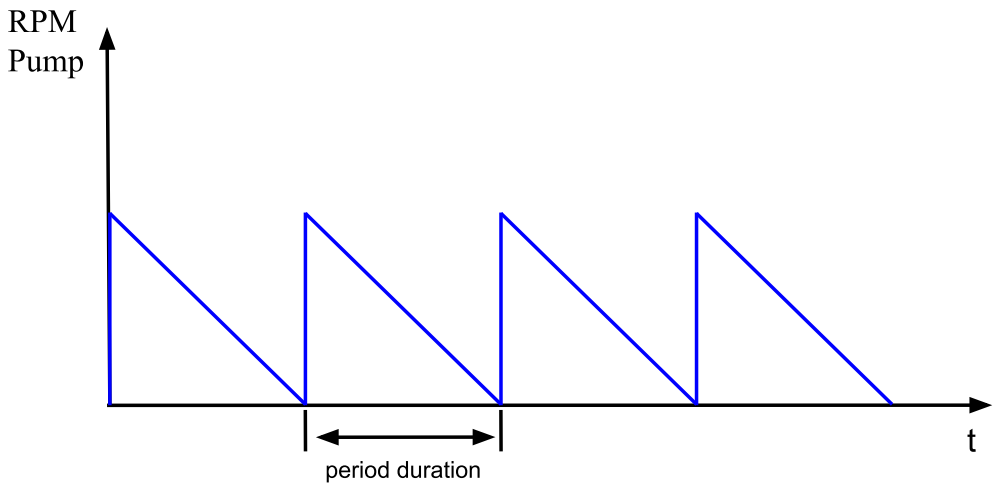

Figure 2.11: For the pump cycle, a sawtooth with a negative ramp was chosen since this waveform is the closest to the flow in the human aorta.

Transparent Polyvinylchlorid (PVC) pipes with a inner diameter of 14mm were used as connection hoses between the reservoir, pump and the phantom. The pipes must be transparent so that the system can be checked for trapped air bubbles since these can influence the flow in the pipe.
To connect the pipe to the reservoir, pump and phantom GARDENA System fittings and cable ties were used.
The aorta phantom was placed in the phantom support setup which consists of a support plate, one inflow and one outflow adapter. The adapter position can be adjusted to fit the length of the aorta phantom by loosening and tightening two M4 nylon screws (MRI compatible). The phantom support and the adapters where modeled using Autodesk, Inc. Fusion 360.
The adapters are manufactured using Basic Resin by 3D-basics printed on the LD-002R printer by Creality [46], [38].
The .stl and .f3d file for the adapters and the support plate can be found in the Appendix [A]. In the Figure 2.12, the support setup is visualized as a rendering.

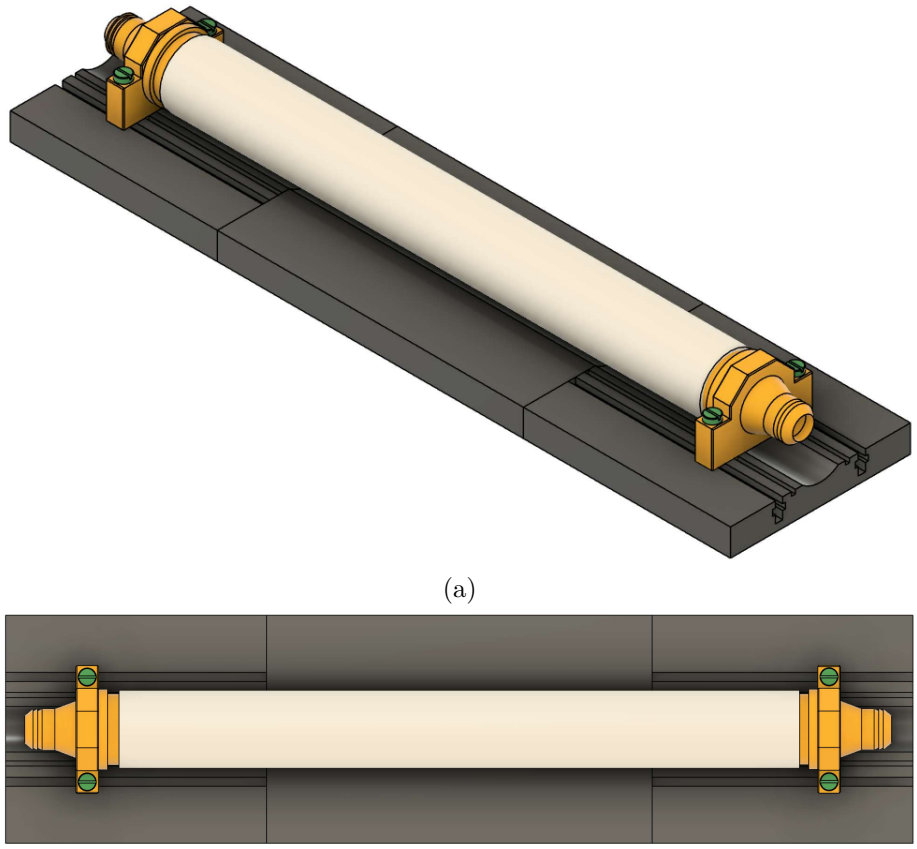

(a)

(b)

Figure 2.12: Rendering of the support setup. (a) top side view and (b) top down view. The support plate is visualized in grey, the adapters in yellow and the aorta phantom in white. The adapters are fixated with four M4 screws (green).

The support setup was placed inside a watertight tub to capture any water leaking from the adapters or the phantom. In case of a rupture of the phantom, a breakage of the adapter or the loosening of the PVC pipe, this container catches the water. It is important that the water volume in the reservoir does not exceed the volume of the tub. This causes the pump to run dry before the tub overflows and avoids any damage to electronic equipment by the the water. Before the measurement can start, it is important to check the setup for any leaks, air bubbles or kinks in the PVC tubes.

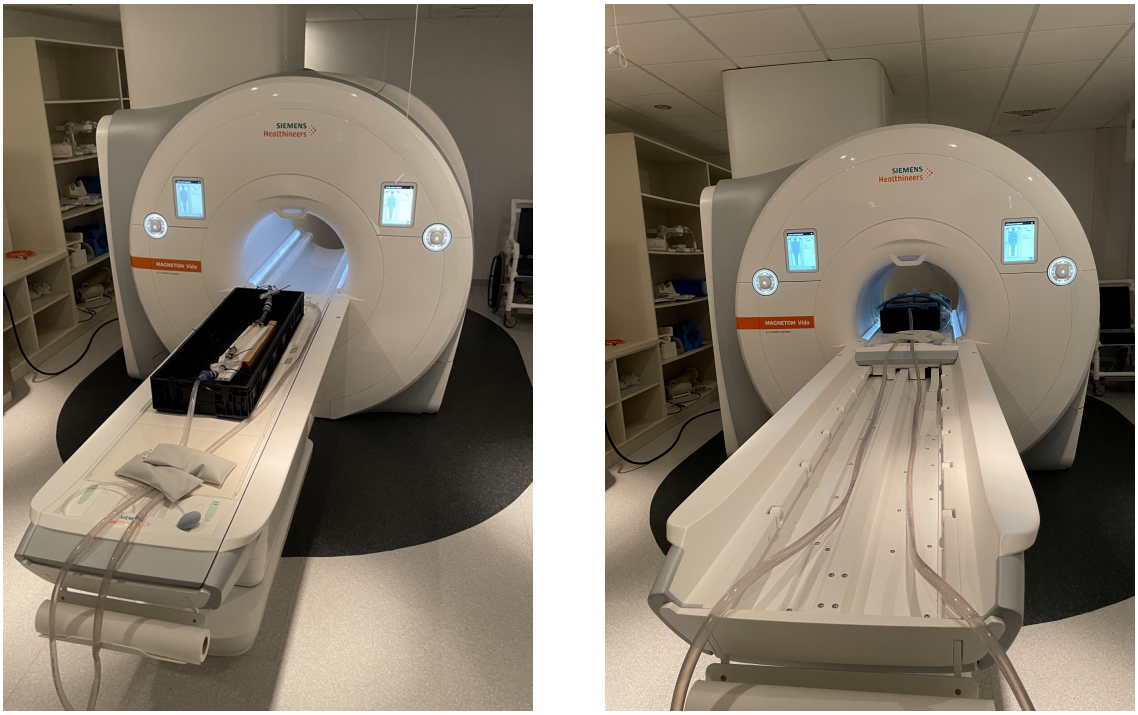

(a) (b)

Figure 2.13: (a) preparation of the measurement box for the MRI flow measurement (b) measurement box in the bore of the MRI.

2.4.2 Ultrasound flow measurement

The Ultrasound (US) flow measurement setup was developed by Manuel Hölzl in the course of his master thesis at the TU Graz [47]. The measurement of the flow is thereby based on the Δ time of flight (ΔToF) method. This method uses the phenomenon that the propagation time of an ultrasonic wave is influenced by the velocity of the medium it is traveling through. US transducers are used to convert electric signals into ultrasonic waves and vice versa. Two transducers are placed before the aorta phantom and two transducers after the phantom to measure the inlet flow and the outlet flow simultaneously. Therefore, the transducers clamped onto the PVC tube using a 3D printed fixture designed and manufactured by Manuel Hözl. The fixture and the transducers are shown in Figure 2.14.

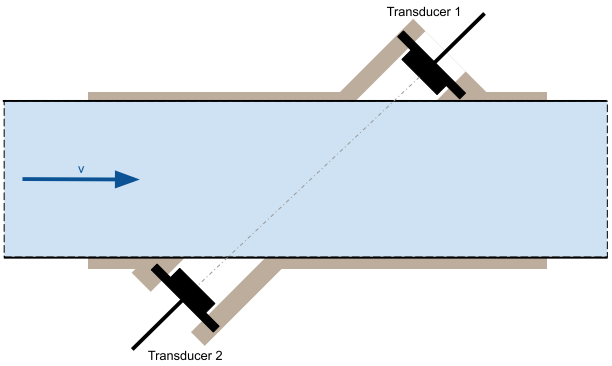

Figure 2.14: Measurement setup for the US flow measurement using the Δ ToF method. Two transducers are used (Transducer 1 and 2) which are clamped onto the PVC pipe which connects the pump with the phantom and the phantom which the reservoir. These US sensors can be placed directly into the bore of the MRI scanner.

Further information regarding the US measurement setup can be found in Manuel Hölzls master thesis *Ultrasound Based Flow Measurement System Suitable for MRI-Environment.*

Data analysis and interpretation

The data preparation and processing can be divided into several blocks, which are run through sequentially to determine the PWV from the raw data. The inflow and outflow flow data was recorded by Manuel Hölzls *USS-Application* software and saved as a comma separated file (*.csv*). In this file, the raw flow data captured by the US setup. In Figure 2.15 the path of the data is visualized starting with the read in of the raw data from the .csv file. The functions used for the interpolation, filtering and peak detection are described in detail in Section 2.4.4.
From this mean inflow and outflow curve and the distance between the phantom adapters the PWV is calculated.

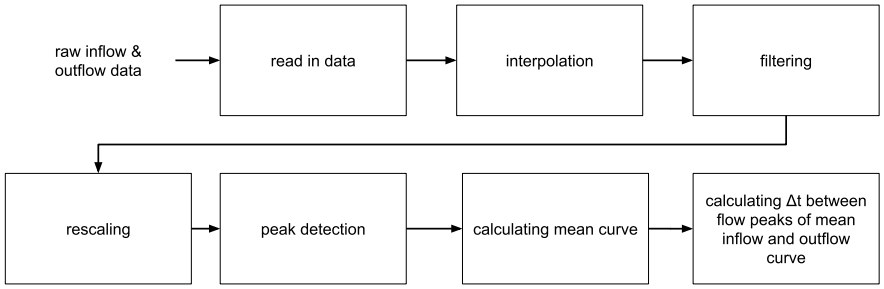

Figure 2.15: Flow chart for calculating the time shift between the inflow curve and the outflow curve from the raw US data.

2.4.3 MRI flow measurement

Triggered radial phase contrast sequence

One approach to determine the flow curve in the inflow and the outflow slice is the triggered PC measurement. The trigger ensures that the measurement of the inflow and outflow slice starts at the same point in the pump cycle. This allows the reconstructed flow curves to be superimposed and the temporal shift at the inflow and outflow can be determined. Therefore, the flow was continuously measured using the US flow measurement setup which was developed by Manuel Hölzl. The trigger signal is generated by comparing the output of the pump to a set threshold at approximately 80% of the peak flow velocity. When the flow velocity exceeds the threshold, the output for the trigger signal is set to high (3.3 V) and vice versa if the flow velocity is below the threshold, the trigger signal is low (0 V).
The trigger signal is converted to an optical signal via a versatile link adapter which is then connected to the MRI System via the optical fiber cable in the control room. The trigger signal is displayed in Syngo (control software of the MRI System) as ”External Trigger 2”.

Interleaved radial phase contrast sequence

The second approach is to measure the flow in the inflow and the outflow slice ”simultaneously”. Thereby, no external trigger is needed. This is achieved by measuring the flow using a interleaved radial sequence. For each slice, 350 spokes are measured while alternating between the slices. This allows the flow curves to be compared directly with each other.

Scanner, sequence setting & image reconstruction

All MRI measurements where made using a Siemens Vida 3 Tesla clinical MRI scanner located at the Technical University Graz, Kopernikusgasse 24 and the sequence settings were made using Siemens Syngo, the standard control software for the Vida MRI scanner [48], [49]. For the reconstruction, the Berkeley Advanced Reconstruction Toolbox (BART) was used with nonlinear inversion (NLINV) as the reconstruction method [50], [51]. The reconstruction script was provided by Philip Schaten from the Technical University Graz, Institute of Biomedical Imaging and can be found in the Appendix [C.1].

In order to determine the number of spokes required for a correct representation of the flow pulse, the same measurement was reconstructed with a series of different spokes per frame. The results shown in chapter 3.3.1 show that the reconstruction with 11 spokes per image represents the true flow curve best. Therefore, all further MRI measurements in this thesis are reconstructed with eleven spokes per frame.
The TR was set to the lowest possible value which was 3.3 ms to achieve the highest possible frame rate.
This leads to a frame time of

$$T_{perFrame} = 3.3 \cdot 11 \cdot 2 = 72,6ms$$

for the triggered PC measurement (see equation (21)) and

$$T_{perFrame} = 3.3 \cdot 11 \cdot 2 \cdot 2 = 145,2ms$$

for the interleaved PC measurement.

Data preparation MRI

The flow data is extruded from the images by calculating the mean over all pixels in the region of interest (ROI).

$$\mu = \frac{1}{N} \sum_{(x,y) \in ROI} f(x,y) \tag{22}$$

where the ROI is composed of N pixels $\{(x_1,y_1),(x_2,y_2), \ldots ,(x_N,y_N)\}$ and f(x,y) is the reconstructed flow image (pixel value describes the flow orthogonal to the image plane).
Doing this for every frame in the time series, this results in a flow curve representing the time dependent flow through the phantom.
The further preparation of the raw flow data is visualized in Figure 2.16. In Section 2.4.4 the interpolation, filtering and the peak detection are described in detail.

After determining that the maximum flow velocity is approximately 50 $cm \cdot s^{-1}$, the v_{enc} was set to 80 $cm \cdot s^{-1}$ for all measurements.

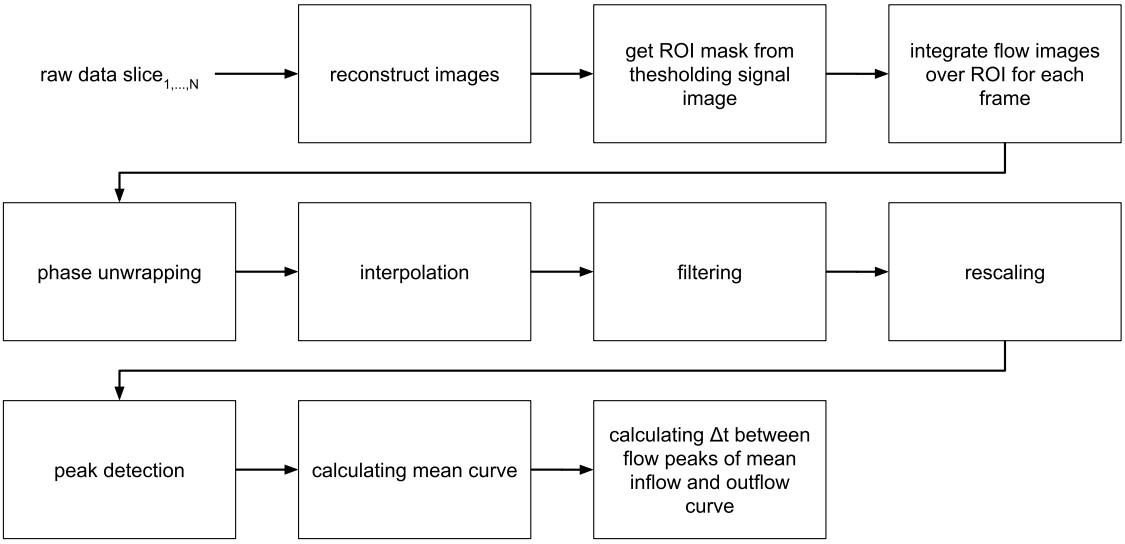

Figure 2.16: Flow chart for calculating the time shift between the inflow curve and the outflow curve from the raw PC MRI data.

Phase unwrapping

Since phase wrapping is prone to happen at the peak of the flow curve (highest flow velocity), it can lead to a shift of the peak along the time axis (flow peak appears to be earlier than it actually is). Since the peak flow velocities at the inflow is naturally higher than at the outflow when using an elastic phantom, this effect is not symmetrical and can therefore lead to a lower PWV (inflow peak shifted to the left & outflow peak correct $\rightarrow$ Pulse transit time higher (PTT) $\rightarrow$ PWV lower) [52].

Region of interest map

The ROI in this case describes the cross section of the phantom. To determine this region first, the mean of all magnitude images over the time series is calculated.

$$\mu(x,y) = \frac{1}{T}\sum_{t=1}^{T} I_t(x,y) \tag{23}$$

To get the ROI from this averaged magnitude image, a simple threshold registration is performed

$$M(x,y) = \begin{cases} 1, & \mu(x,y) \geq \tau \\ 0, & \mu(x,y) < \tau \end{cases} \tag{24}$$

where

$$\tau = x * max(\mu(x,y)) \tag{25}$$

and x being determined by visual inspection of the resulting ROI.

2.4.4 Flow data preparation US & MRI

Interpolation

To improve the accuracy when determining the flow peak, the data is interpolated to a sampling rate of 1 kHz. This is done by using *interp1d* by scipy. The interpolation type is set to cubic which refers to a interpolation of third order.

Filtering

The flow signal is filtered using a butterworth filter from scipy. The filter parameters are set so that the filter functions as low pass filter with an order of two and a cut off frequency (3 dB frequency) of 1.5 times the pulse frequency.

Peak detection

For the peak detection, the function *find_peaks* from scipy signal is used. This function returns the peaks of a given input signal. In addition to the required input signal, a number of optional parameters can be given. In this case, the additional parameter distance was used and set to 80% of the pulse length. This parameter sets the minimal distance between two neighboring peaks.

2.4.5 Determine PWV from flow data

To calculate the PWV from the recorded flow data, two different approaches where used. On the one side, the peak-to-peak (PTP) calculation and on the other side, the mean curve calculation.

Peak-to-peak

In the peak-to-peak approach, every peak in the flow data of the outflow is coupled to one peak in the inflow data. Then the time shift between each peak couple is calculated. For the peak detection, the *find_peaks* function from scipy was used. With the distance between the measurement points and the time shifts over all peaks, the mean PWV is calculated.
This approach was used for the US measurement and the interleaved MRI measurement since in these setups the data for the inflow and the outflow were recorded simultaneously. The implemented algorithm can be found in the Appendix [C.3].

Mean curve

For the mean curve approach, the inflow data is analyzed and the peaks in the inflow data are determined using the *find_peaks* function from scipy. Then, a window is generated by selecting the data points 500 ms prior to the peak and the 800 ms after the peak. The corresponding data points in the outflow data is selected and then a mean inflow curve and a mean outflow curve is calculated. This approach has the advantage that even if the peaks in the outflow data can not be determined correctly due to a bad signal to noise ratio, the PWV can be calculated.

An example:

- Peak in the inflow data is at i=1600 ms
- The window begins at i_{start}=1100 ms and ends at i_{end}=2400 ms
- All inflow data points in the window 1100 ms to 2400 ms are selected
- All outflow data points in the window 1100 ms to 2400 ms are selected
- This is repeated for all inflow peaks
- A mean inflow and a mean outflow curve is calculated from the selected inflow and outflow data

With the mean inflow and outflow curves, the PWV is calculated from the time shift of the flow peaks and the distance between the measurement points. The implemented algorithm can be found in the Appendix [C.3].

2.5 Simulation

The simulation of the propagation of pulse wave was done with the svFSI package which is part of the open source simulation toolbox SimVascular which was implemented by Stanford Medicine University, Berkeley University of California, OSMSC and the University of Texas ar Austin [53]. SvFSI is a multi-physics finite element solver developed for computational modeling of the cardiovascular system. It provides a wide range of capabilities, including the simulation of cardiac electrophysiology, biological tissue mechanics, blood flow and large-deformation fluid structure interaction (FSI). In addition, svFSI supports a variety of boundary conditions, enabling patient specific modeling of cardiovascular biomechanics.
The solver is parallelized using the message passing interface and offers multiple options for linear solvers and preconditioners. SvFSI can be utilized either as an integrated component of the SimVascular software, or as in this thesis, as a standalone solver [54].

2.5.1 Settings

The references to the mesh files and the settings for the simulation are stored in an input file with the file extension *.inp*. The used .inp file can be found in the Appendix [D]. The main settings that have to adjusted are the time step, the references to the *.vtu* and *.vtp* files (meshes), the linear solver type, the boundary conditions and the material properties.

Time steps

Via testing various different step sizes for the simulation, 1 ms appeared to be the sweet spot between the required time resolution for determining the PWV accurately, a stable simulation (longer time steps can lead to not converging simulations) and computing costs.

Boundary conditions

The input and output boundary conditions were determined by calculating the dynamic pressure via the flow velocity in the phantom.

$$p_{dynamic} = \frac{\rho \cdot v}{2} \tag{26}$$

For the inlet, the water has a velocity of approximately 50 $cm \cdot s^{-1}$ what leads to a dynamic pressure of around 125 Pa. For the outlet, the water has a mean velocity of approximately 12 $cm \cdot s^{-1}$ what leads to a dynamic pressure of around 7.2 Pa. These maximum flow velocity were determined by analyzing the reconstructed flow images pixel wise.
For the inlet function, a step function with a step at t=0 was chosen.

2.5.2 Model and mesh

For generating the model and the mesh for the FSI simulation, the open source 3D finite element mesh generator GMSH was used [55].
The wall thickness and the radius of the lumen was set to be the same as in the physical model (wall thickness 2 mm, radius 15 mm, see chapter 2.3). To reduce the calculation time, the length for the vessel was reduced from 300 mm in the physical phantom to 100 mm.
A tetrahedral mesh model was generated for the lumen and the fluid domain and exported as a *.vtk* file and then spit up in individual *.vtu* and *.vtp* files to create the directory required for the svFSI simulation.
The corresponding mesh files can be found in the Appendix [D]. The material properties (E-modulus and Poisson's ratio) are set to match the in the UAT determined values.

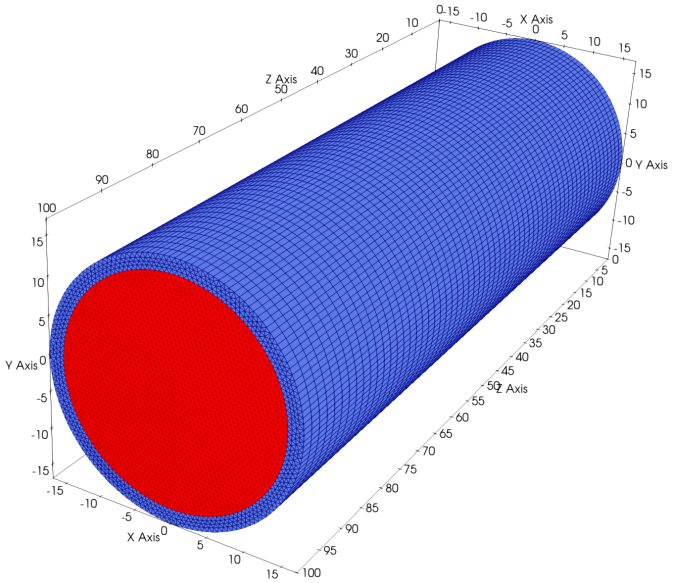

Figure 2.17: Rendering of the meshed model with the fluid in red and the lumen in blue (dimensions in mm).

To define the boundary conditions, the model was divided into two volumes and seven surfaces. For each of these volumes and surfaces, an individual *.vtu* or *.vtp* file was generated. The files are organized in a directory which is visualized in the Figure 2.18.

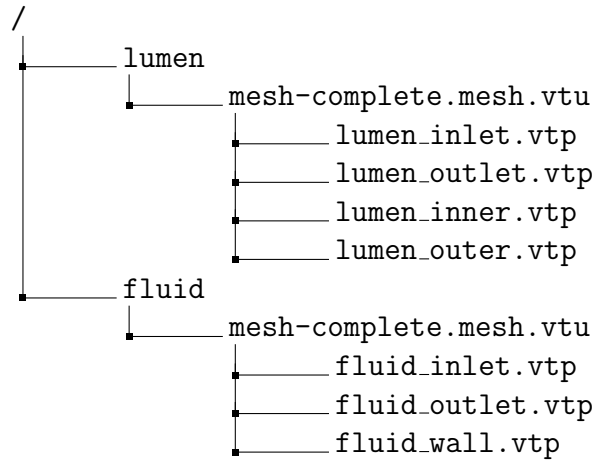

Figure 2.18: The model was split up into the lumen (vessel wall) and the fluid. The lumen has four surfaces (inlet, outlet, inner wall and outer wall) and the fluid has three surfaces (inlet, outlet and surface to the lumen wall).

2.5.3 Computing

For computing the simulation generalized minimal residual method was chosen as the linear solver type with *FSILS* as the preconditioner.
The simulation was executed using the following terminal command in the same directory as the created .inp file.

mpirun -np 4 /Path/to/svFSI/build/svFSI-build/bin/svFSI
The calculation was done using a private MacBook Pro 2015 with 16 GB RAM.
One simulation took approximately 5 hours.

2.5.4 Visualization

The simulation result is saved as a series of *.vtu* and a corresponding .bin file, where each *.vtu* and *.bin* couple represent a simulation time step. These results are visualized and analyzed using ParaView 5.13.2, which is an open source software that is based on the Visualization Toolkit.

3 Results

In the following chapter, the results of the UAT, US measurement, PC MRI measurement and the simulation results are visualized and presented. Furthermore, the result of the pulse frequency dependent PWV measurement is displayed.

3.1 Results UAT

The results of the UAT are shown in the Figures 3.1 and 3.2. The calculated E-modulus and Poisson's ratio is shown in the Table 2. The corresponding raw data for the following plots can be found in the Appendix [E.3] and the used algorithms for the data analysis in Appendix [C.2].

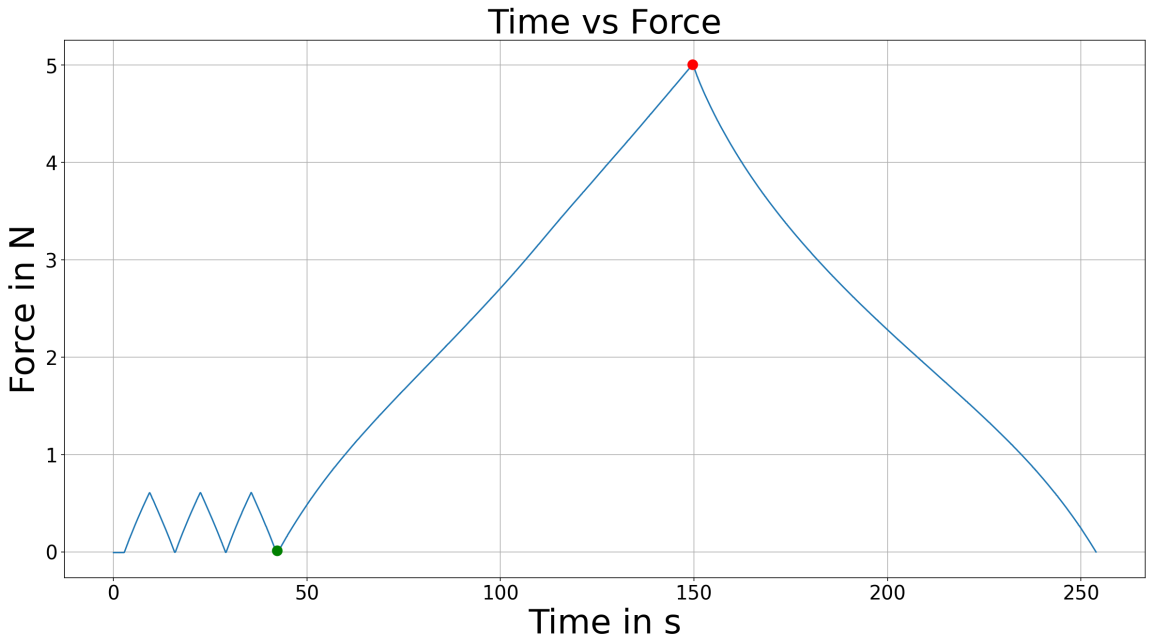

Figure 3.1: Raw test data saved by the UAT control software. The force is measured by the load cell and the pull speed is controlled via the actuators. The three small peaks on the left are the precondition cycles. The data used for determining the mechanical properties of the materials is between the green and the red dot (final pull).

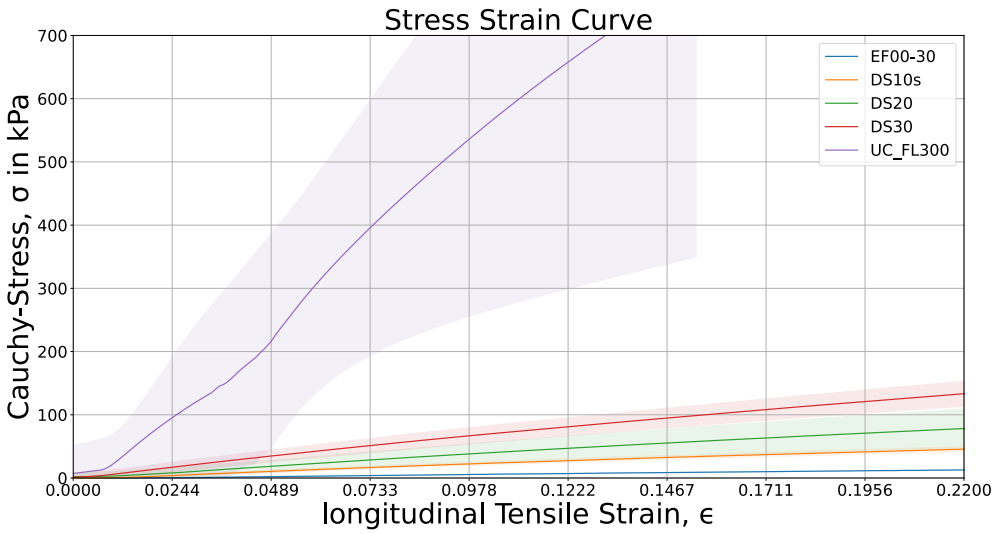

Figure 3.2: The results of the UAT is displayed in a Stress-Strain plot where the incline of the curve represents the E-modulus of the material. It can be seen, that the flexible UV-Resin UC FL300 has a high variance in terms of elasticity since the purple area is large in comparison to the other materials. Furthermore, this material is significantly stiffer (steeper incline of the stress strain curve) than the other materials.

The UAT was repeated for ten samples per material divided up into multiple batches to check whether the material properties are consistent.

Table 2: Results of the UAT for the chosen materials.

Material	**E-modulus** in kPa	**Poisson's ratio**
EF00-30	53 ± 2.95	0.273 ± 0.03
DS10S	147 ± 13.95	0.42 ± 0.06
DS20	327 ± 154.80	0.43 ± 0.18
DS30	569 ± 94.89	0.49 ± 0.05
FL300	4657 ± 3161	0.43 ± 0.03

During the preparations for the flow measurements using the 3D printed phantoms manufactured out of Stratasys tissue matrix both, the horizontally and the diagonally printed phantom experienced a material failure. In Figure 3.3, the material failure is shown in detail. As a result, no US and MRI flow measurements could be conducted with this material. Therefore, no UATs were performed with the Stratasys tissue matrix.

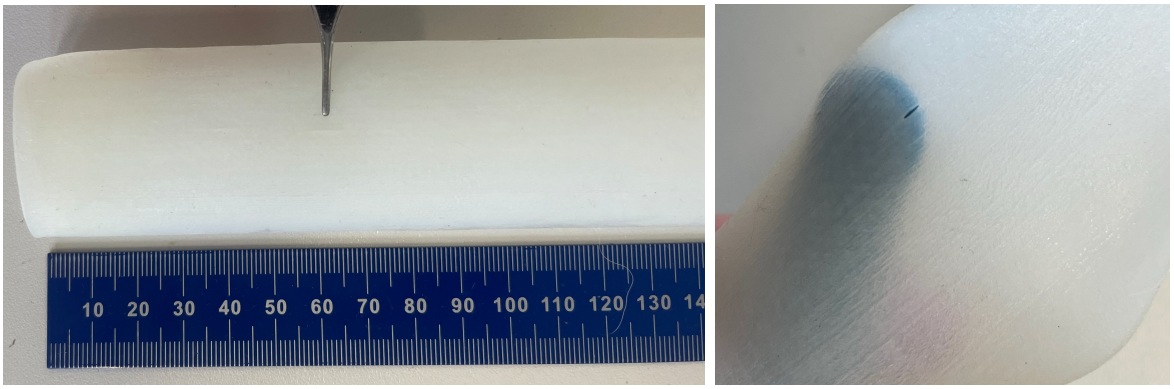

(a) (b)

Figure 3.3: The aorta phantoms manufactured from Stratasys tissue matrix experienced a material failure. a) shows the location of the failure and b) a close up of the hole that emerged during the preparatory test.

The UATs of the flexible resin show that the material is very stiff when compared to the 2k-silicon samples. Furthermore, the UATs of this material indicate a high degree of variation in the individual samples and thus a high standard deviation. For these reasons and the fact that it is difficult to manufacture an uniform phantom with the given equipment, the flexible resin was not taken into account in further tests.

3.2 Results of the analytical calculation

In the Table 3, the results of the calculated PWV using the Moens-Korteweg equation (7) and the modified Moens-Korteweg equation (8) are displayed. As for the E-modulus and the Poisson's ratio, the material properties determined by the UAT were used (see 2).

Table 3: Results of the analytical calculation of the expected PWV using the Moens-Korteweg equation and the modified Moens-Korteweg equation

Material	**Moens-Korteweg Eq.** in $m \cdot s^{-1}$	**modified Moens-Korteweg Eq.** in $m \cdot s^{-1}$
EF00-30	1.86 ± 0.02	1.91 ± 0.07
DS10S	3.07 ± 0.14	3.38 ± 0.27
DS20	4.45 ± 1.25	5.05 ± 1.67
DS30	6.05 ± 0.67	6.87 ± 0.65
FL300	15.93 ± 7.08	17.34 ± 7.44

3.3 Results of the US flow measurement

In this section, the results of the US flow measurements are shown. Figure 3.4 visualizes the raw flow data recorded with the US flow measurement setup from Manuel Hölzl. Since the US measurement setup is designed to measure volume flow the results for the US measurement is displayed as a volume flow rate. In Figure 3.5, the filtered signal and the calculated flow peaks are show. From the temporal distance between the corresponding inflow and outflow peaks and the distance between the US transducers, the PWV shown in the Table 4 was calculated. The distance between the US sensors was determined to be 300 mm since the distance between the adapters was approximately 300 mm. The corresponding raw data for the following plots can be found in the Appendix [E.1] and the used algorithms for the data analysis in Appendix [C.3].

3.3.1 Raw flow data from the US flow measurement

The raw flow data of the US measurement visualized in Figure 3.4 shows clear peaks in the inflow flow curve with a fast up slope and a graduate down slope. In the outflow curve, the peaks are dampened but still recognizable. A phase shift between the inflow and outflow flow curves can be seen.

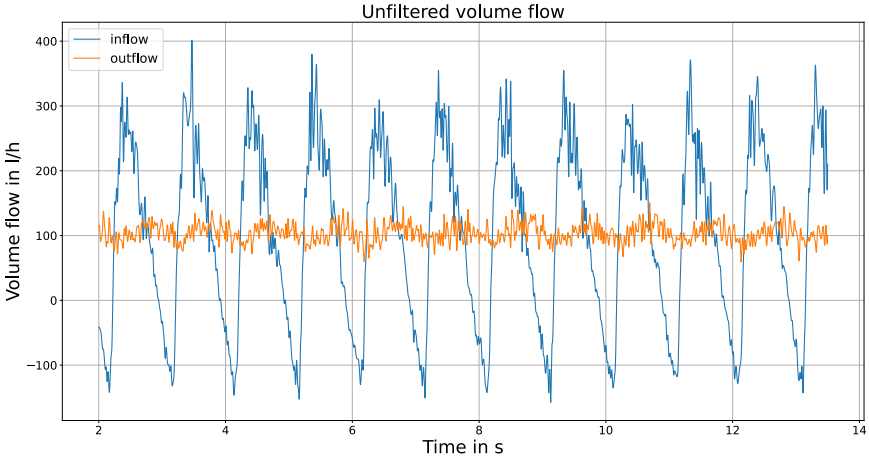

Figure 3.4: Unfiltered volume flow data in l/h collected by the US flow measurement setup. The outflow is clearly dampened when compared to the inflow which has distinct peaks. At the inflow the set pump profile can be clearly observed.

3.3.2 Filtered flow data from the US flow measurement

Filtering the raw US data leads to distinct peaks in the inflow and outflow flow curves. Due to the butterworth filter, the maximum flow volume is reduced from approximately 300 l/h to approximately 170 l/h in the inflow slice.

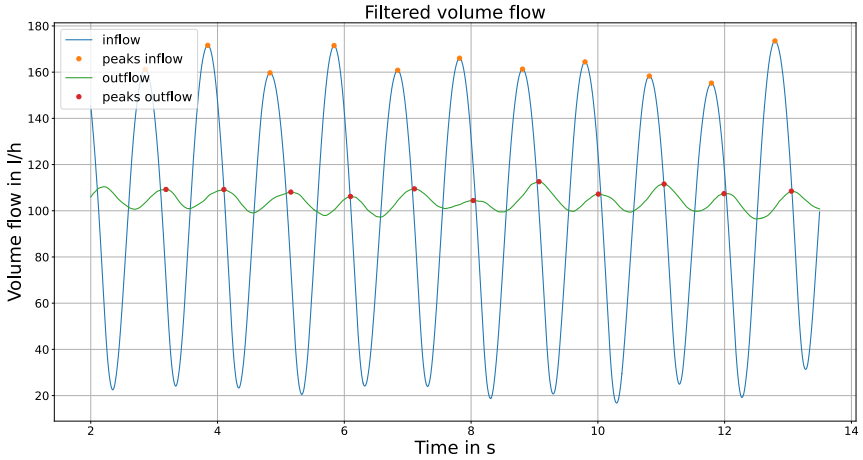

Figure 3.5: US flow data for a pump periode of one second filtered using the butterworth filter butter from scipy signal. The filter parameters were set so that the resulting filter is of order 2 and hast a cutoff frequency of 1.5 Hz. The peaks of the inflow and outflow data is marked using find_peaks from scipy signal (see 2.4.4)

3.3.3 PWV result from the US flow measurement

In order to exclude the possibility that the adapters or the US setup lead to a delay of the pulse wave, a ”zero” phantom measurement was performed. This was done by placing the adapters directly in line with each other and sealing small gap with a short piece of flexible resin. No time shift in the flow peaks could be observed and thus it can be assumed that the adapters have no influence on the time shift and the US setup has no influence on the measured PWV in the phantoms.
In the Table 4, the results for the PWV in the DS20 and DS30 phantoms using the US measurement setup are listed.

Table 4: Results of the US flow measurement for the chosen materials

Material	**Peak shift** in ms	**PWV** in $m \cdot s^{-1}$
DS20	328 ± 76	1.07 ± 0.43
DS30	269 ± 47	1.3 ± 0.26

3.4 Results of the PC MRI PWV measurement

The corresponding raw data for the following plots can be found in the Appendix [E.2] and the used algorithms for the data analysis in Appendix [C.3].

3.4.1 Sequence settings

To set the number of spokes used in the reconstruction for one frame correctly the same measurement is reconstructed using a series of different spoke numbers per frame and then the outcome is compared. This test is shown in Figure 3.6.

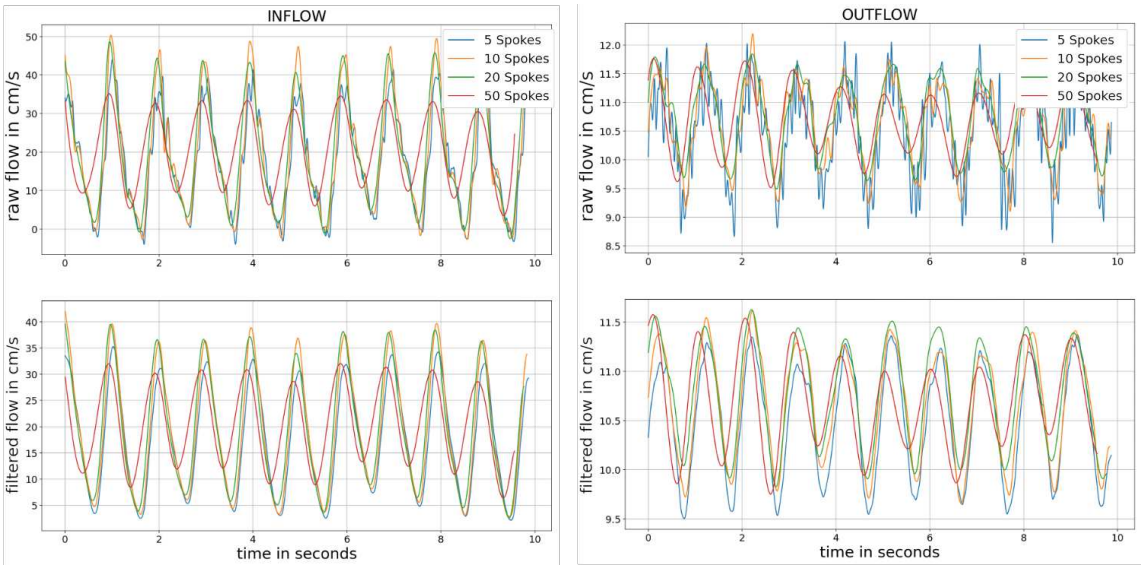

Figure 3.6: To determine the number of spokes needed, the inflow and outflow slice was reconstructed with various numbers of spokes per frame. The most accurate representation of the true flow is the green curve which represents the reconstruction with 10 spokes.

3.4.2 Raw PC MRI image

In Figure 3.7, one frame reconstructed using 11 spokes is shown. The flow phantom can be seen in the middle of the frame. Radial streak artifacts can be seen around the phantom.

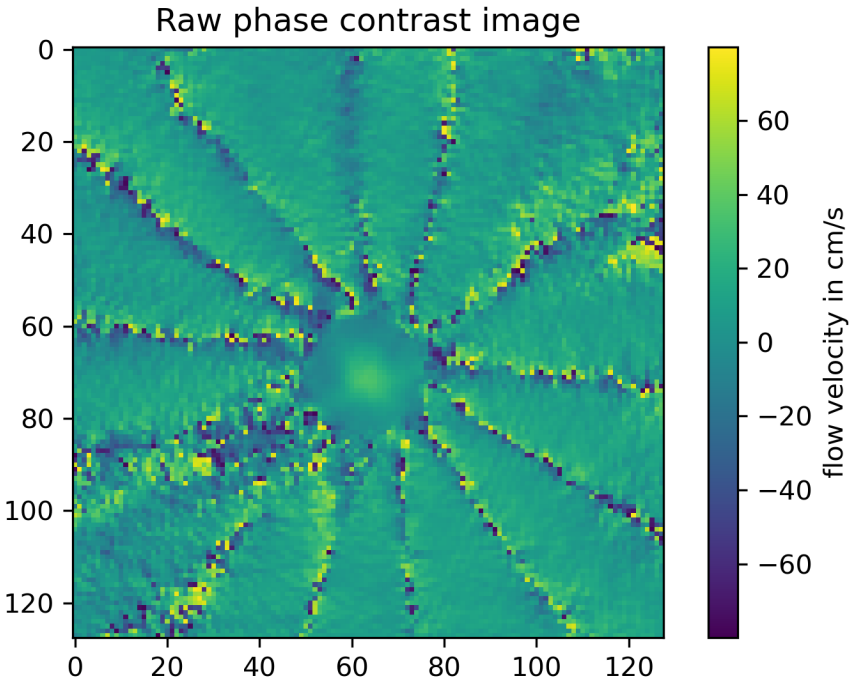

Figure 3.7: Raw phase contrast image of the inflow slice. This measurement was done using an aorta phantom manufactured from DS30. The phantom can be observed as a circle in the center of the image where the flow velocity is the highest in the center and the lowest at the lumen wall. Around the phantom, severe streaking artifacts can be seen.

3.4.3 Calculated ROI map

Figure 3.8 shows the resulting ROI map calculated by averaging all the magnitude images of a slice and applying a threshold of 70% of the maximum magnitude.

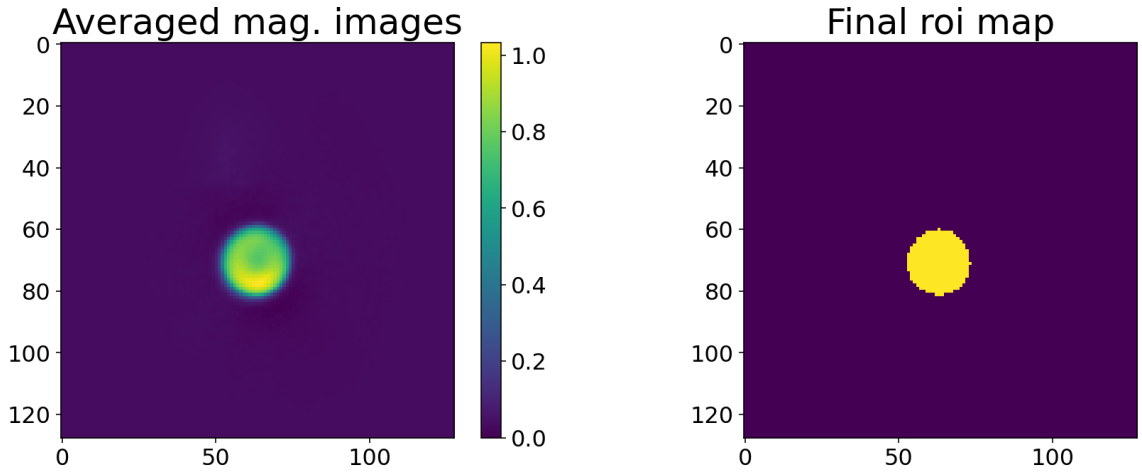

Figure 3.8: On the left hand side, the averaged magnitude image for the inflow slice is shown and on the right hand side the resulting ROI map can be seen. In this example, the measurement was done using an aorta phantom manufactured from DS30.

3.4.4 Flow data from the PC MRI measurement

In Figure 3.9 and Figure 3.11, the raw flow data for the triggered and interleaved PC MRI measurement of the DS30 phantom is show. For this measurement, the pump was set to a period of one second. For the triggered PC measurement, the peak velocity through the inflow slice measured by averaging over the ROI is 20 cm $\cdot$ s^{-1}. In the interleaved PC MRI measurement, the peak velocity is 14 cm $\cdot$ s^{-1}. In the outflow slice, the peak velocities are 12 cm $\cdot s^{-1}$ (triggered) and 8.5 cm $\cdot$ s^{-1} (interleaved).

The velocity data is filtered using the scipy signal butterworth filter with a cutoff frequency of 2 Hz is visualized in Figure 3.10 for the triggered PC MRI measurement and in Figure 3.12 for the interleaved PC MRI measurement.

Triggered radial PC MRI sequence

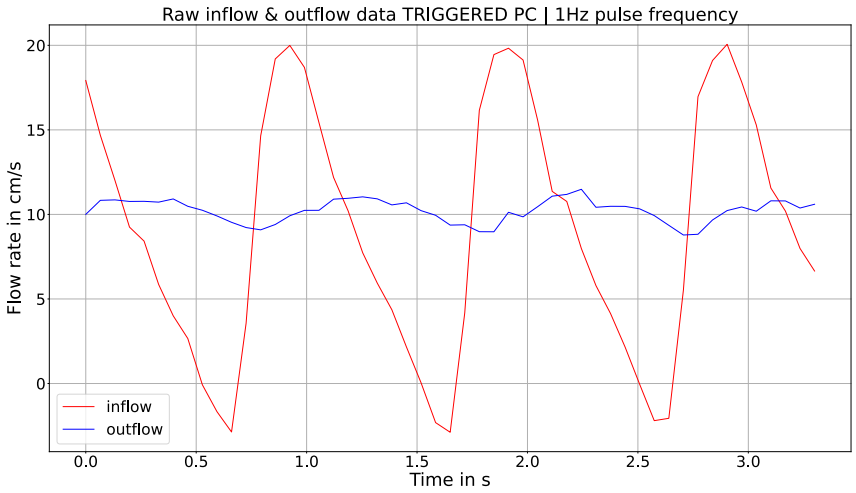

Figure 3.9: Raw flow velocity data from a triggered radial PC sequence for a pump period of one second. This measurement was done using an aorta phantom manufactured from DS30.

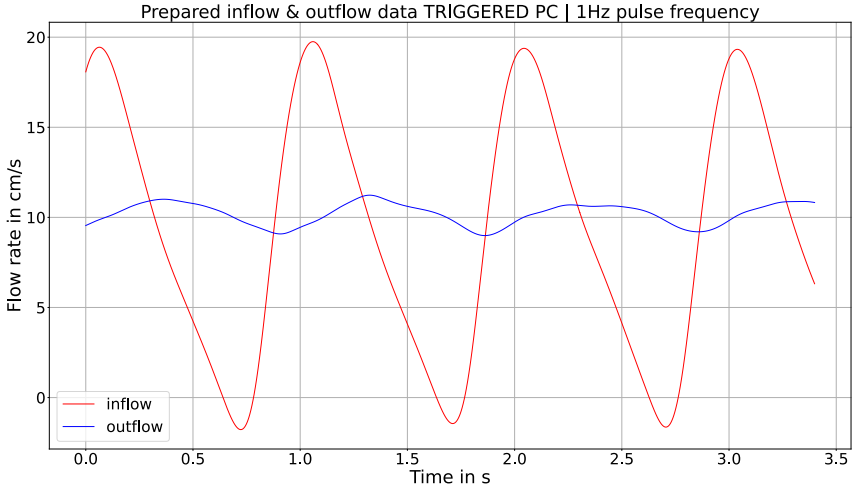

Figure 3.10: The raw flow velocity data from the triggered radial PC MRI sequence visualized in Figure 3.9 is filtered using the scipy butterworth filter with a cutoff frequency of 2 Hz to get the filtered flow velocity data for the PWV calculation. In this measurement the pump period was set to one second and the aorta phantom manufactured from DS30 was used.

Interleaved radial PC MRI sequence

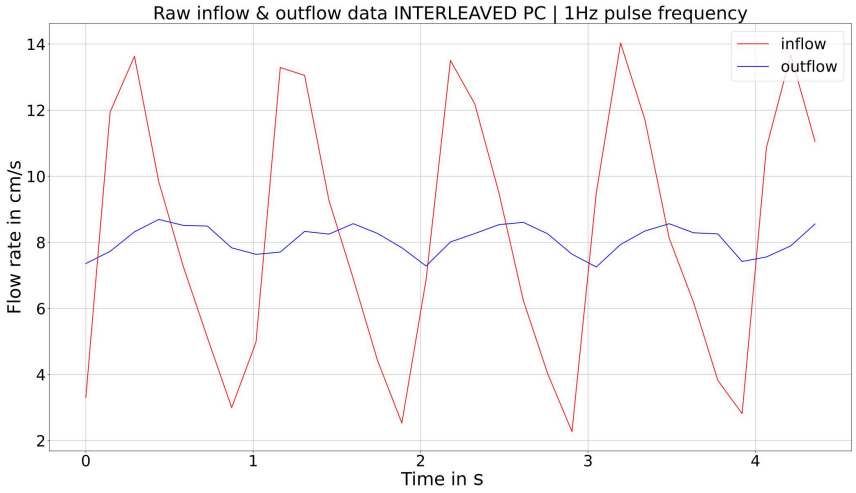

Figure 3.11: Raw flow velocity data from an interleaved radial PC sequence for a pump period of one second. This measurement was done using an aorta phantom manufactured from DS30.

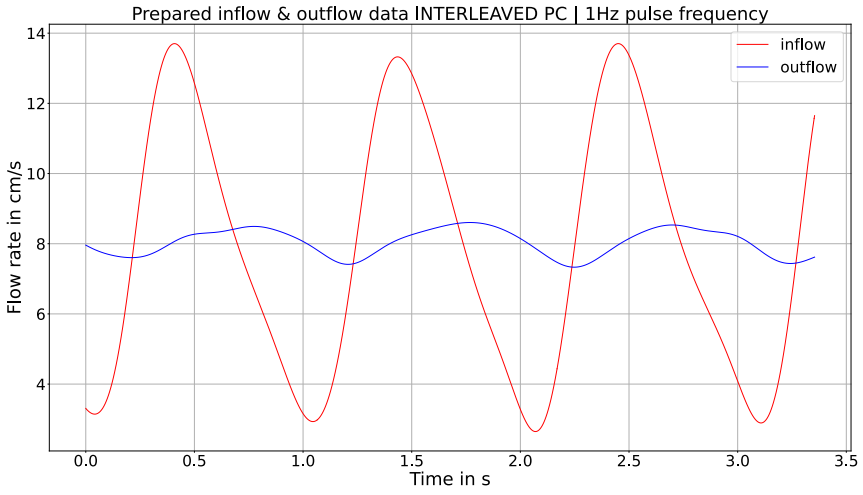

Figure 3.12: To prepare the raw flow velocity data from the interleaved radial PC sequence for the PWV calculation the scipy butterworth filer with a cutoff frequency of 2 Hz is used (pump period of one second). This measurement was done using an aorta phantom manufactured from DS30.

3.4.5 PWV calculation peak-to-peak PC MRI

In Figure 3.13, the peaks in the inflow and the outflow flow velocity curves resulting from the filtered interleaved PC MRI measurement are displayed. From the temporal distance between an inflow peak and a corresponding outflow peak and the slice positions, the PWV is calculated. The distance between the slices was set to approximately 300 mm (exact slice position was taken into account).

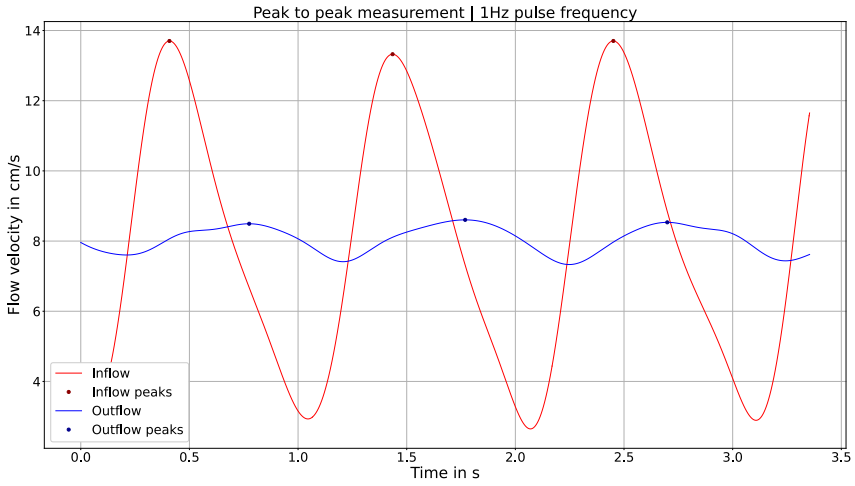

Figure 3.13: To calculate the PWV from the interleaved measurement the time shift between the inflow peak and the outflow peak is determined. From this shift and the slice positions (approximately 300 mm), the PWV is calculated.

Table 5: Result of the peak-to-peak PWV measurement using interleaved PC MRI and the DS20 and DS30 aortic phantom.

Material	**Peak shift** in ms	**PWV** in $\mathrm{m} \cdot \mathrm{s}^{-1}$
DS20	182 ± 7	1.66 ± 0.06
DS30	188 ± 48	1.75 ± 0.35

3.4.6 PWV calculation mean curve PC MRI

The mean flow velocity curve in the inflow and outflow slice resulting from the triggered PC MRI measurement is shown in Figure 3.14. From time shift between the inflow and the outflow flow curve and the distance between the slices, the PWV is calculated. The distance between the slices was set to approximately 300 mm (exact slice position was taken into account). These results are listed in Table 6.

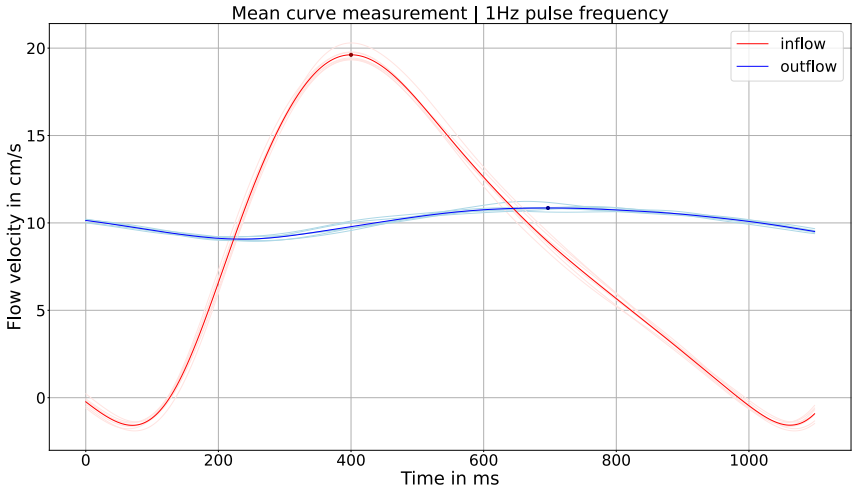

Figure 3.14: From the triggered PC sequence the mean curve for the inflow and outflow slice is calculated. Thereby, the signal to noise ratio is greatly improved. This measurement was done using an aorta phantom manufactured from DS30.

Table 6: Result of the mean curve PWV measurement using triggered PC MRI and the DS20 and DS30 aortic phantom.

Material	**Peak shift** in ms	**PWV** in $m \cdot s^{-1}$
DS20	243 ± 14	1.24 ± 0.07
DS30	227 ± 25	1.32 ± 0.15

3.5 svFSI simulation results

In Figures 3.15 and 3.16, the results of the FSI simulation is visualized. To estimate the PWV from the simulation results, the pressure along the middle axis of the phantom is plotted (see Figure 3.16). Then, the time steps it takes the pulse wave to travel through the phantom and the phantom length are used to calculate the PWV. From the time it takes the pressure wave to reach the end of the phantom and the length of the phantom, the PWV, shown in Table 7, is calculated.

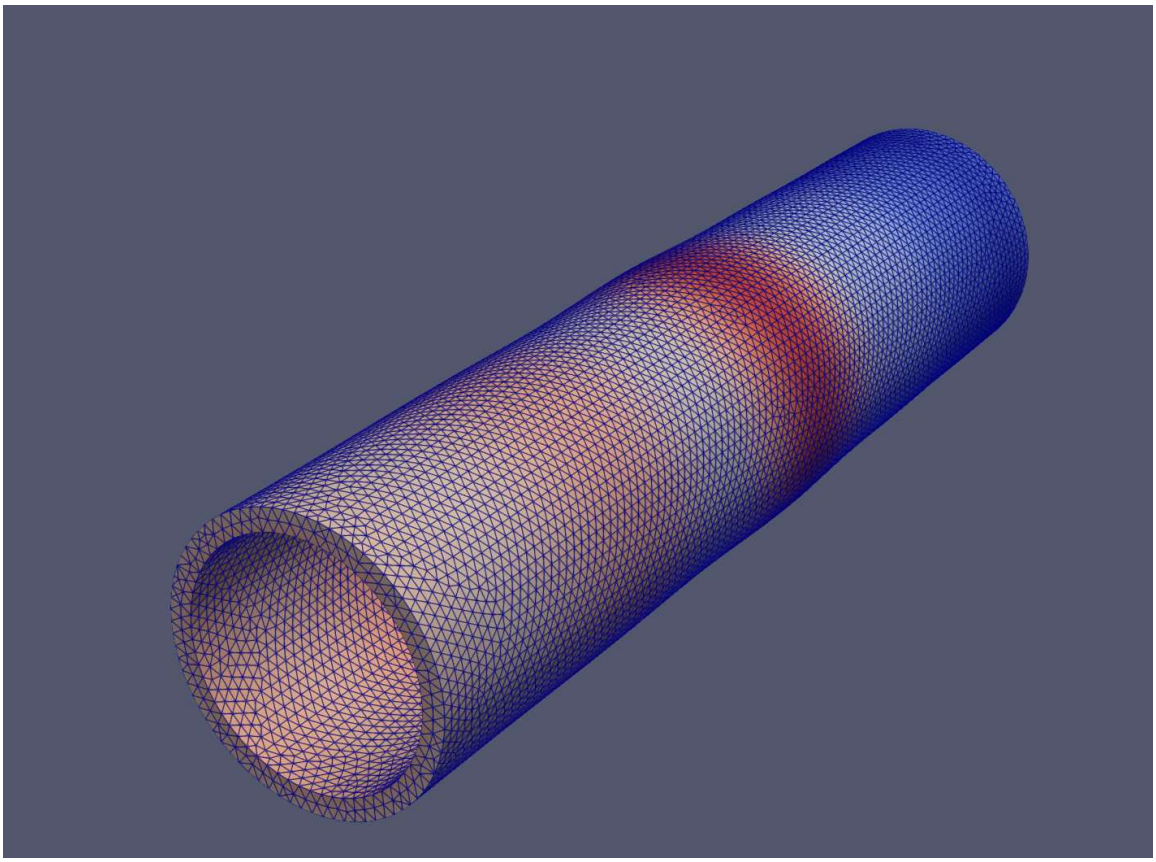

Figure 3.15: To visualize the spatial displacement of the lumen wall by the fluid pressure, the deformation is shown on a color scale. Red indicates a strong deformation, blue indicates no deformation.

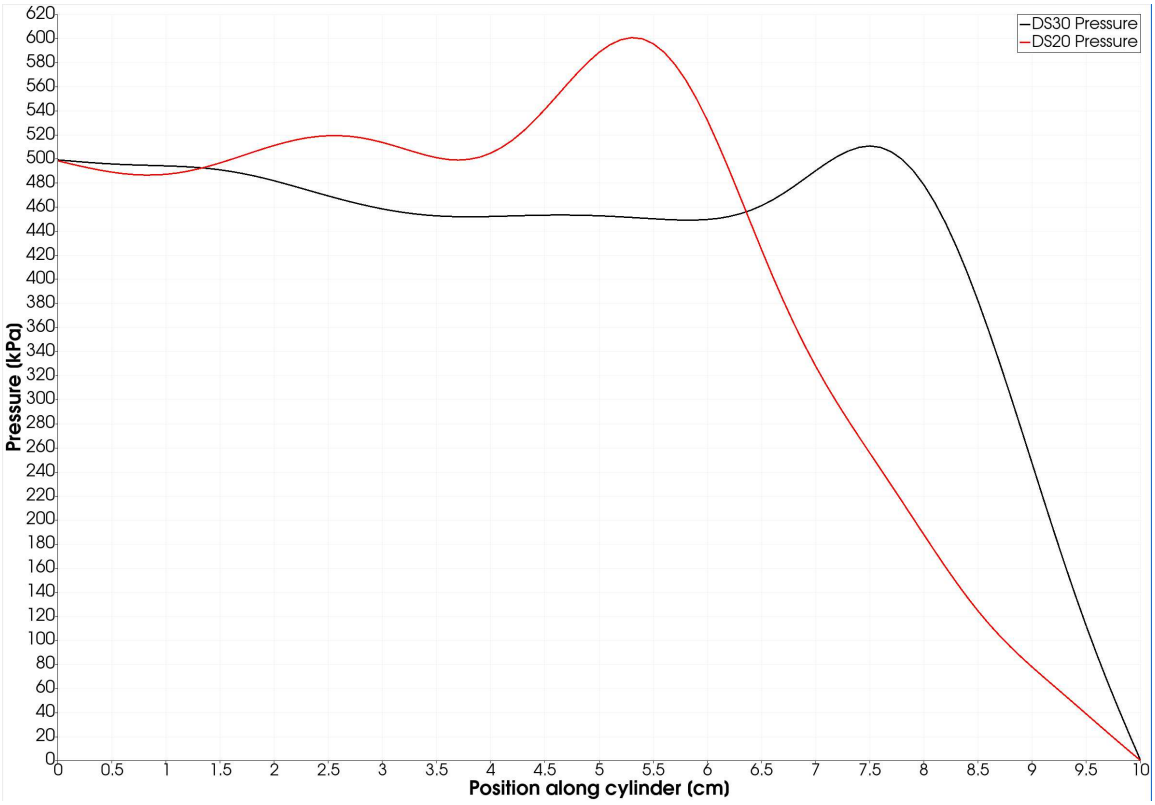

Figure 3.16: To visualize the pressure along the lumen, the pressure along the centerline of the vessel is plotted. In black, the FSI simulation result of the stiffer DS30 is visualized. In red, the result for the softer DS20 is shown. It can be seen that the pressure wave propagates faster in the softer DS20 phantom when compared to the DS30 phantom because the pressure peak in the DS30 phantom propagated further in the same time when compared to the DS20 phantom.

Table 7: Results for the PWV from the FSI simulation

Material	**PWV** in $\mathrm{m} \cdot \mathrm{s}^{-1}$
DS20	1.28
DS30	1.75

3.6 Frequency dependent PWV measurement results

In this Section, the results for the PWV measurement for pulse time are shown. This measurement performed by increasing the pump period from 500 to 1200 ms in 100 ms increments. The corresponding raw data for the following plots can be found in the Appendix [E.1] and [E.2] as well as the used algorithm for the data analysis in Appendix [C.3].

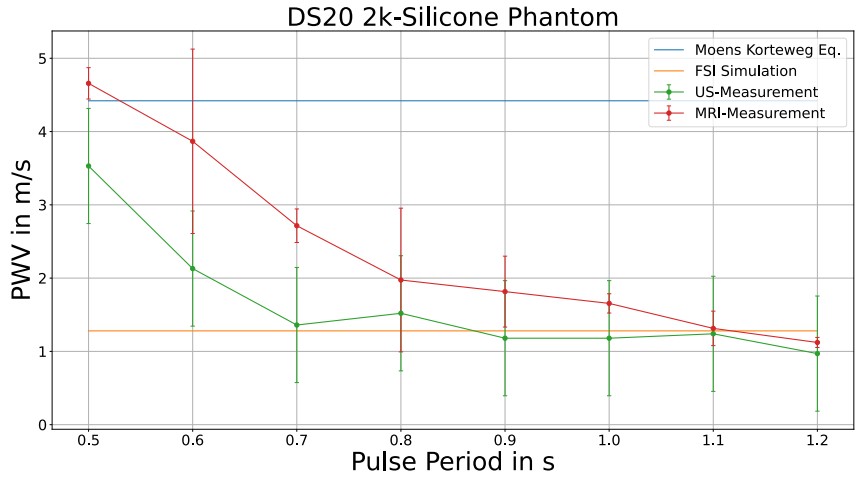

(a)

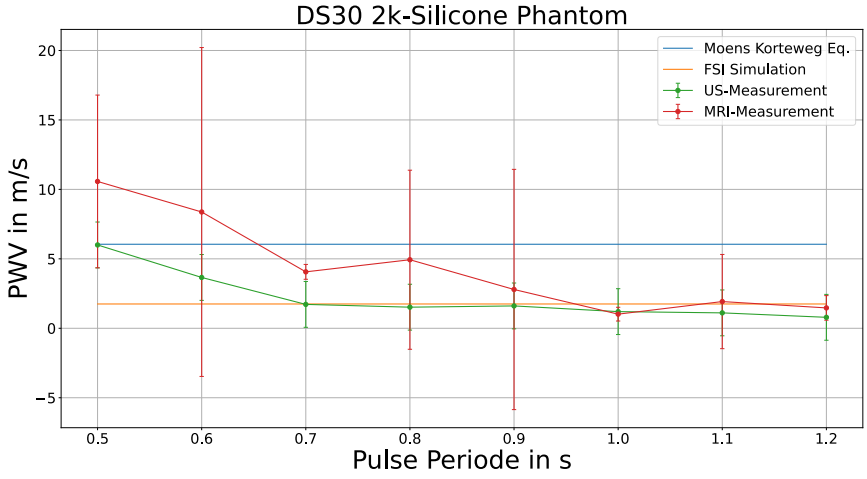

(b)

Figure 3.17: To investigate the effect of pulse frequency on the PWV, measurements were conducted using interleaved PC MRI and US. The pulse period was systematically varied from 0.5 seconds to 1.2 seconds in increments of 0.1 seconds. The results indicate a strong dependence of PWV on the pulse period, with higher pulse frequencies (i.e., shorter pulse periods) resulting in significantly increased PWV values.

4 Discussion

The results of the performed UAT (see Table 2 in the results section) show that the manufactured UAT samples have similar mechanical properties as specified by the manufacturer in the data sheets. The E-modulus of DS20 was stated by the manufacturer to have an E-modulus of 338 kPa. In the UATs, the DS20 has shown to have an E-modulus of 327 kPa. For the DS30 the from Smooth On, Inc. stated E-modulus is 593 kPa and the calculated E-modulus is 569 kPa. Therefore, it can be said that the 2k-silicones are processed correctly. No significant difference in the mechanical properties were found between the batches and it can thus be assumed that the phantoms manufactured from the materials have the same properties as the UAT samples. The modulus of elasticity of the 2k-silicones DS20 and DS30 is within a range that is suitable for the manufacture of flow phantoms for measuring PWV. As can be seen in the results, the samples made from the flexible resin UC-FL300 showed high variance in terms of E-modulus. In addition, the E-modulus of this material exceeds the target range.
The Stratasys tissue matrix material represented a potentially suitable option for the fabrication of vascular phantoms, as it is reported by the manufacturer to exhibit mechanical properties comparable to those of human blood vessels. In addition to its mechanical characteristics, the material offers considerable flexibility in manufacturing, enabling the production of not only simple straight tubular structures, but also anatomically more realistic vascular geometries, including curved vessels (e.g., the aortic arch), branched structures (e.g., renal arteries) and bifurcations (e.g., the aortic bifurcation). Such capabilities could facilitate the development of flow phantoms that more closely replicate physiological vascular conditions. However, the Stratasys Tissue Matrix material was not used in this work due to practical limitations encountered during manufacturing. In particular, insufficient layer adhesion was observed during the printing process, which compromised the structural integrity of the fabricated vessel. Additionally, the relatively high material costs represented a further limitation.
The from the mechanical properties and the geometry of the phantom calculated PWV using the Moens-Korteweg equation show an analytically determined PWV of
4.45 $m \cdot s^{-1}$ for the DS20 phantom and a PWV of
6.05 $m \cdot s^{-1}$ for DS30 phantom. Using the modified Moens-Korteweg equation an PWV of 5.05 $m \cdot s^{-1}$ for the DS20 and 6.87 $m \cdot s^{-1}$ for the DS30 phantom was calculated. Since the modified Moens-Korteweg equation takes the wall thickness into account, it can be concluded that the PWV calculated via the modified equation is more precise.

The results of the PWV measurement using the US flow measurement setup presented in the Table 4 show a significantly lower PWV when compared to the analytical approach. Furthermore, the PWV in the DS30 phantom is only slightly higher than in the softer DS20 phantom. Comparing the PWV determined by the triggered and the interleaved PC MRI flow measurement shows that both measurement approaches give very similar values for both the DS20 and DS30 phantoms. For the interleaved measurement, the setup is significantly simpler and faster to set up and therefore it is used for the measurement of the frequency dependent PWV. In the raw data it can be seen that the triggered measurement achieves a sampling time is twice as high as the interleaved measurement.

The PWV measured using the US setup (1.3 $m \cdot s^{-1}$ for the DS30) is comparable to the triggered PC MRI measurement (1.32 $m \cdot s^{-1}$) with the interleaved PC MRI measurement the resulting PWV is 1.75 $m \cdot s^{-1}$. An explanation for this discrepancy could be the higher sampling rate of the interleaved measurement. At the same time, the PWV obtained from the flow measurements is approximately 4.7 times lower than the PWV calculated using the Moens–Korteweg equation.
One possible explanation for the discrepancy in the PWV results is that the Moens–Korteweg equation relies on a number of simplifying assumptions and reduces the highly complex phenomenon of wave propagation in elastic tubes to a comparatively simple analytical expression. While the equation provides a useful approximation, it was originally developed to describe pulse wave propagation in the human arterial system under specific physiological conditions. In vivo, arterial walls are typically subjected to a certain level of pretension due to the baseline blood pressure, which influences their effective stiffness and, consequently, the propagation speed of the pressure wave. In addition, the arterial system is not an isolated tube but is connected to a complex network of peripheral vessels that contribute to the overall compliance of the vascular system. These effects can alter the propagation characteristics of the pulse wave and are not captured by the simplified model. Furthermore, the surrounding tissue in the human body may mechanically constrain the vessel and thereby influence its deformation behavior during pulse propagation. Finally, the viscosity and rheological properties of blood may introduce additional damping and energy dissipation effects, which are typically neglected in the classical formulation of the Moens–Korteweg equation.
An explanation for the offset of the determined PWV using US and PC MRI is the difference in the sampling time and the measurement points. The PC MRI has a sampling time of approximately 145 ms versus 15 ms with the US setup. This could lead to a more precise measurement of the peak flow, which in turn has an effect on the PWV. In addition, the US setup measures the flow before and after the adapters in the PVC pipe which could lead to a compression of the flow curve when compared to the PC MRI measurement where the slices were placed between the adapters (beginning and end of the phantom).
Furthermore, the adapters used to fixate the phantom and the distance between the pump and the phantom can influence the development and propagation of the pulse wave by acting like a nozzle.
Another important aspect concerns the determination of the temporal shift between the flow curves. In this work, the peak of the flow curve was consistently used as the reference point for this determination. However, temporal stretching or compression of the flow curves at the inflow or outflow can influence the measured time shift between the curves and, consequently, affect the calculated PWV.
During the measurements, it was also observed that the flow phantom was sucked out due to the inertia of the water. This was successfully counteracted by installing a valve at the outlet to the reservoir. However, it is possible that this phenomenon could not be completely eliminated, which could also lead to a distortion of the results.
The evaluation of the svFSI FSI simulation and the resulting PWV yields results similar to those of the PWV of the US and MRI measurements. The stiffer DS30 phantom leads to a PWV of 1.75 $m \cdot s^{-1}$ and the softer DS20 phantom to an PWV of 1.28 $m \cdot s^{-1}$. This indicates that the simulation slightly overestimates the PWV. This can be due to the

limited mesh size and the restrictions regarding the time step size. To test the effect of the boundary conditions, these conditions and the input pressure at t=0 where altered. Indicated by the Moens-Korteweg equation, the pressure has no significant influence on the propagation speed of the pulse wave.
In summary, the comparison of the different measurement methods show that the measurements and the simulation lead to a comparable PWV. However, further investigations are necessary to determine the exact causes why the PWV calculated using the Moens-Korteweg equation and the modified Moens-Korteweg equation are significantly higher.
The measurement of the PWV as a dependence of the pump frequency using the US flow measurement setup shows a near parabolic increase of the PWV when increasing the pump frequency from 1 Hz to 2 Hz. The same phenomenon can be observed in the MRI measurement. At a pulse time of 500 ms, the with the MRI setup measured PWV of the DS20 phantom is almost equal to the calculated PWV using the Moens-Korteweg equation. The pulse frequency dependent PWV measurement in the DS30 phantom shows a high variance at a pulse period of 0.6 seconds and 0.9 seconds. For the low pulse periods, the sampling time of the PC MRI measurement might also have an effect on the measured PWV since the peaks of the flow curves are not accurately determined.
The same effect was observed in studies that have investigated the influence of heart rate on PWV in the human body [56]. The results indicate that the mechanical response of the vessel wall is dependent on the pulse frequency. Until today, the influence of an increased pulse rate on the PWV is not fully understood [5], [57].

4.1 Conclusion

This thesis covers the complete workflow from the material selection all the way to the comparison of the PWV results encompassing a wide variety of areas including CAD modeling, mechanical testing, various manufacturing processes, data preparation, data analysis to answer the research question: What level of agreement and systematic differences exist between pulse wave velocity values determined using US flow measurements, MRI flow measurements, analytical models, and fluid–structure interaction simulations in aortic phantoms?

Starting with the mechanical testing which was necessary for selecting suitable materials for for the PWV measurements. From a number of materials, two were successfully selected for the manufacturing of flow phantoms. An efficient and reproducible workflow was developed with which phantoms can be produced in house using relatively simple equipment. Various US and PC MRI flow measurements were successfully performed using the phantoms. To determine the PWV from these measurements, the relevant flow data was extracted and processed using data analysis. The in the first step determined mechanical properties were used to on the one hand compute a fully coupled FSI simulation to determine the PWV and on the other hand to calculate the PWV using the Moens-Korteweg equation and the modified Moens-Korteweg equation. Thereby, the PWV for a given material was determined using five different methods which allows a comparison of these methods.
In addition, it was shown that the setup is potentially suitable for the in dept investigation

of the effect of the pulse frequency on the PWV since the setup allows for an easy adjustment of the pulse frequency and outflow pressure.
In the course of this master thesis, a wide variety of disciplines were successfully combined to investigate the effect of the mechanical properties of materials on PWV as well as the comparability of different measurement methods, FSI simulation, and analytical calculations of PWV.

4.2 Outlook and further research

The flow tests revealed a number of potential adaptions that can be done to further improve the measurements. Starting with the pump used for the tests. The used pump has a predefined RPM curve. Changing this pump to a programmable pump would allow for an optimized flow profile (set time between the pump strokes, set slope of ramp up and ramp down). A different pump may also allow for a faster ramp up time resulting in a sharper peak which would simulate the fast opening of the aortic valve in the human body. Another potential improvement would be to add a synthetic aortic valve. Similar to the human body, this valve would allow for a sudden pulse wave but even more critical, it would suppress backflow which potentially has a significant effect on the PWV. To further improve the setup, the flow phantom could be submerged underwater or surrounded by soft silicone to mimic the human body. The viscosity of the fluid may also influence the measured PWV. Here, a water-glycol mixture could be used to imitate the viscosity of real blood.
Furthermore, to simulate the real mechanical properties of the human aorta (non-linear elasticity,...) there is still much development to be done in the field of material science. By further developing the 2k-silcone mold, the aorta can be replicated more realistically. Various branches of blood vessels and the aortic arch might have a major influence on how the pulse wave propagates and thus also on PWV.
In regard of the PC MRI measurement, the sampling time may be reduced by adjusting the number of spokes. Further testing is necessary to validate whether 5 or 7 spokes used to reconstruct one frame may result in a more precise measurement of the PWV.
The measurement of the PWV using the US setup could be improved by for example designing a new adapter between the PVC tube and the phantom into which the transducers are directly installed. This would prevent the PVC tube from interfering with the ultrasound waves and could potentially improve the signal-to-noise ratio leading to a more precise measurement of the flow curve. Further possible improvements regarding the US setup are listed in the master thesis from Manuel Hölzl.
By changing the input function from a simple step function to for example a falling sawtooth function it would be possible to simulate the effect of the puls frequency in the FSI simulation. This would require significantly higher computing power, but would more accurately represent real-world flow experiments.
The aspects discussed above indicate that the experimental setup can be further improved in several respects. Nevertheless, the setup developed within the scope of this work provides a solid foundation for such improvements and for further investigations of pulse wave propagation in controlled environments. In order to establish PWV measurements using MRI in clinical practice, the validation of the derived PWV values represents a critical step. Experimental setups, such as the one presented in this thesis, enable a direct

comparison of different measurement techniques and thereby allow their performance and reliability to be systematically evaluated. Such validation is essential to ensure that MRI-based PWV measurements provide accurate and reproducible results.
As mentioned in the introduction, cardiovascular diseases remain one of the leading causes of mortality worldwide. Consequently, gaining a deeper understanding of the complex mechanisms affecting pulse wave propagation in the human vascular system is of considerable importance. In particular, the influence of physiological factors such as vessel wall elasticity, vascular geometry, blood viscosity, and pulse frequency on the PWV is of significant scientific and clinical interest. In vivo measurements make it difficult to isolate the influence of these individual parameters. Controlled phantom setups therefore play an important role, as they allow specific parameters to be varied independently while keeping other conditions constant. This enables a more systematic investigation of the mechanisms governing pulse wave propagation and their impact on PWV.

Appendices

Appendix A: 3D Models

UAT sample mold:
Appendix/Models/UAT_sample_mold.stl
Appendix/Models/UAT_sample_mold.f3d

UAT dogbone model:
Appendix/Models/UAT_dogbone_model.stl
Appendix/Models/UAT_dogbone_model.f3d

Phantom mold:
Appendix/Models/phantom_mold.stl
Appendix/Models/phantom_mold.f3d

Phantom model:
Appendix/Models/phantom_model.stl
Appendix/Models/phantom_model.f3d

Phantom adapters:
Appendix/Models/phantom_adapters.stl
Appendix/Models/phantom_adapters.f3d

Phantom support plate:
Appendix/Models/phantom_support_plate.stl
Appendix/Models/phantom_support_plate.f3d

Appendix B: Documents

B.1 UAT Test protocol

Appendix/UAT/UAT_test_protocol.pdf

Appendix C: Algorithms

C.1 Reconstruction Script by Philip Schaten, Technical University Graz, Institute of Biomedical Imaging

Read raw data:
Appendix/Algorithms/MRI_Reconstruction/read.sh

Reco script:
Appendix/Algorithms/MRI_Reconstruction/reco_11Sp.sh

PC flow calculation:
Appendix/Algorithms/MRI_Reconstruction/calc_flow.sh

Main script:
Appendix/Algorithms/MRI_Reconstruction/run.sh

C.2 Data extraction and analysis UAT

Appendix/Algorithms/data_analysis_UAT/data_analysis_UAT.py

C.3 PWV tools

Spoke comparison:
Appendix/Algorithms/MRI_Reconstruction/Spoke_comparison.py
PWV tools:
Appendix/Algorithms/data_analysis_PWV/pwv_tools_V2.py

Frequency dependent PWV:
Appendix/Algorithms/data_analysis_PWV/frequency_dependent_PWV.py

Data analysis interleaved PC MRI.py:
Appendix/Algorithms/data_analysis_PWV/data_analysis_interleaved_PC-MRI.py

Data analysis triggered PC MRI.py:
Appendix/Algorithms/data_analysis_PWV/data_analysis_triggered_PC-MRI.py

Data analysis US.py: Appendix/Algorithms/data_analysis_PWV/data_analysis_US.py

Appendix D: FSI Simulation

Mesh model:
FSI_simulation/mesh

Simulation file:
Appendix/FSI_simulation/2025-05-04_svFSI.inp

Appendix E: Measurement data

E.1 US measurement data

US measurement:
Appendix/Measurement_data/US/2025-05-05_US/

US measurement frequency dependent:
Appendix/Measurement_data/US_data/2025-07-10_frequency_dependent_PWV_US/

E.2 PC MRI measurement data

PC MRI measurement spoke selection:
Appendix/Measurement_data/MRI_data/2025-04-16_spoke_selection_PC-MRI/

PC MRI triggered measurement:
Appendix/Measurement_data/MRI_data/ 2025-04-16_triggered_PC-MRI/

PC MRI interleaved measurement:
Appendix/Measurement_data/MRI_data/2025-06-25_interleaved_PC-MRI/

PC MRI measurement frequency dependent:
Appendix/Measurement_data/MRI_data/2025-07-11_frequency_dependent_PWV_PC-MRI/

E.3 UAT data

Appendix/Measurement_data/UAT_data/

References

[1] N. W, 'McDonald's Blood Flow in Arteries,' *Theoretical, Experimental and Clinical Principles*, vol. 67, pp. 321–337, 2005. [Online]. Available: https://cir.nii.ac.jp/crid/1570291226078369920.

[2] S. Laurent *et al.*, 'Aortic Stiffness Is an Independent Predictor of All-Cause and Cardiovascular Mortality in Hypertensive Patients,' *Hypertension*, vol. 37, no. 5, pp. 1236–1241, 2001, ISSN: 0194911X. DOI: 10.1161/01.HYP.37.5.1236. [Online]. Available: /doi/pdf/10.1161/01.HYP.37.5.1236?download=true.

[3] H. Sato, J. Hayashi, K. Harashima, H. Shimazu and K. Kitamoto, 'A population-based study of arterial stiffness index in relation to cardiovascular risk factors,' *Journal of atherosclerosis and thrombosis*, vol. 12, no. 3, pp. 175–180, 2005, ISSN: 1340-3478. DOI: 10.5551/JAT.12.175. [Online]. Available: https://pubmed.ncbi.nlm.nih.gov/16020919/.

[4] V. V. Bonarjee, 'Arterial Stiffness: A Prognostic Marker in Coronary Heart Disease. Available Methods and Clinical Application,' *Frontiers in Cardiovascular Medicine*, vol. 5, p. 64, Jun. 2018, ISSN: 2297055X. DOI: 10.3389/FCVM.2018.00064. [Online]. Available: https://pmc.ncbi.nlm.nih.gov/articles/PMC6008540/.

[5] J. Liu, B. An, B. Shi, X. Li and L. Qian, 'Influence of Blood Pressure and Heart Rate on PWV Measurement: Assessment Under Real-Time Blood Pressure Monitoring,' *Physiological Research*, vol. 73, no. 6, p. 963, 2024. DOI: 10.33549/physiolres.935372. [Online]. Available: www.biomed.cas.cz/physiolresPhysiol.Res.73:963-971,2024https://doi.org/10.33549/physiolres.935372.

[6] G. Fiori, F. Fuiano, A. Scorza, S. Conforto and S. A. Sciuto, 'Non-Invasive Methods for PWV Measurement in Blood Vessel Stiffness Assessment,' *IEEE Reviews in Biomedical Engineering*, vol. 15, pp. 169–183, 2022, ISSN: 1941-1189. DOI: 10.1109/RBME.2021.3092208. [Online]. Available: https://ieeexplore.ieee.org/abstract/document/9464721%20files/408/Fiori%20et%20al.%20-%202022%20-%20Non-Invasive%20Methods%20for%20PWV%20Measurement%20in%20Blood%20.pdf%20files/409/9464721.html.

[7] L. M. Resnick, D. Militianu, A. J. Cunnings, J. G. Pipe, J. L. Evelhoch and R. L. Soulen, 'Direct Magnetic Resonance Determination of Aortic Distensibility in Essential Hypertension,' *Hypertension*, vol. 30, no. 3, pp. 654–659, 1997, ISSN: 15244563. DOI: 10.1161/01.HYP.30.3.654. [Online]. Available: https://www.ahajournals.org/doi/10.1161/01.HYP.30.3.654.

[8] B. D. Bolster, E. Atalar, C. J. Hardy and E. R. McVeigh, 'Accuracy of Arterial Pulse-Wave Velocity Measurement Using MR,' *Journal of magnetic resonance imaging : JMRI*, vol. 8, no. 4, p. 878, Jul. 1998, ISSN: 10531807. DOI: 10.1002/JMRI.1880080418. [Online]. Available: https://pmc.ncbi.nlm.nih.gov/articles/PMC2396309/.

[9] E. D. Lehmann, J. R. Parker, K. D. Hopkins, M. G. Taylor and R. G. Gosling, 'Validation and reproducibility of pressure-corrected aortic distensibility measurements using pulse-wave-velocity Doppler ultrasound,' *Journal of biomedical engineering*, vol. 15, no. 3, pp. 221–228, 1993, ISSN: 0141-5425. DOI: 10.1016/0141-5425(93)90118-I. [Online]. Available: https://pubmed.ncbi.nlm.nih.gov/8320981/.

[10] E.-S. H. Ibrahim, K. R. Johnson, A. B. Miller, J. M. Shaffer and R. D. White, 'Measuring aortic pulse wave velocity using high-field cardiovascular magnetic resonance: comparison of techniques,' *Journal of Cardiovascular Magnetic Resonance*, vol. 12, no. 1, p. 26, 2010, ISSN: 1532-429X. DOI: 10.1186/1532-429X-12-26. [Online]. Available: https://doi.org/10.1186/1532-429X-12-26.

[11] C. D. Fang, 'The cardiac cycle,' *Anaesthesia & Intensive Care Medicine*, vol. 13, no. 8, pp. 391–396, Aug. 2012, ISSN: 1472-0299. DOI: 10.1016/J.MPAIC.2012.05.010. [Online]. Available: https://www.sciencedirect.com/science/article/pii/S1472029912001427.

[12] A. J. Weinhaus and K. P. Roberts, 'Anatomy of the Human Heart,' *Handbook of Cardiac Anatomy, Physiology, and Devices: Second Edition*, pp. 59–85, 2009. DOI: 10.1007/978-1-60327-372-5{_}5. [Online]. Available: https://link.springer.com/chapter/10.1007/978-1-60327-372-5_5.

[13] N. Westerhof, J. W. Lankhaar and B. E. Westerhof, 'The arterial windkessel,' *Medical and Biological Engineering and Computing*, vol. 47, no. 2, pp. 131–141, Jun. 2009, ISSN: 01400118. DOI: 10.1007/S11517-008-0359-2/TABLES/2. [Online]. Available: https://link.springer.com/article/10.1007/s11517-008-0359-2.

[14] Z. M. Fang, X. Feng, Y. Chen, H. Luo, D. S. Jiang and X. Yi, 'Targeting autophagy in aortic aneurysm and dissection,' *Biomedicine & Pharmacotherapy*, vol. 153, p. 113 547, Sep. 2022, ISSN: 0753-3322. DOI: 10.1016/J.BIOPHA.2022.113547. [Online]. Available: https://www.sciencedirect.com/science/article/pii/S0753332222009362#bib1.

[15] H.-P. Elsässer, *Allgemeine Histologie: Ein Kursbegleiter für Humanbiologen mit Atlasteil*. Springer Berlin Heidelberg, 2021, ISBN: 978-3-662-63328-1.

[16] C. R. T. di Gioia, A. Ascione, R. Carletti and C. Giordano, 'Thoracic Aorta: Anatomy and Pathology,' *Diagnostics 2023, Vol. 13, Page 2166*, vol. 13, no. 13, p. 2166, Jun. 2023, ISSN: 2075-4418. DOI: 10.3390/DIAGNOSTICS13132166. [Online]. Available: https://www.mdpi.com/2075-4418/13/13/2166/htm%20https://www.mdpi.com/2075-4418/13/13/2166.

[17] J. A. Collins, J. V. Munoz, T. R. Patel, M. Loukas and R. S. Tubbs, 'The anatomy of the aging aorta,' *Clinical Anatomy*, vol. 27, no. 3, pp. 463–466, Apr. 2014, ISSN: 1098-2353. DOI: 10.1002/CA.22384. [Online]. Available: /doi/pdf/10.1002/ca.22384%20https://onlinelibrary.wiley.com/doi/abs/10.1002/ca.22384%20https://onlinelibrary.wiley.com/doi/10.1002/ca.22384.

[18] J. Blacher, R. Asmar, S. Djane, G. M. London and M. E. Safar, 'Aortic Pulse Wave Velocity as a Marker of Cardiovascular Risk in Hypertensive Patients,' *Hypertension*, vol. 33, no. 5, pp. 1111–1117, 1999, ISSN: 0194911X. DOI: 10.1161/01.HYP.33.5.1111. [Online]. Available: /doi/pdf/10.1161/01.HYP.33.5.1111?download=true.

[19] D. Žikić and K. Žikić, 'Wave propagation through a viscous fluid-filled elastic tube under initial pressure: theoretical and biophysical model,' *European biophysics journal : EBJ*, vol. 51, no. 4-5, pp. 365–374, Jul. 2022, ISSN: 1432-1017. DOI: 10.1007/S00249-022-01604-1. [Online]. Available: https://pubmed.ncbi.nlm.nih.gov/35618857/.

[20] T. Tillin, J. Chamvers, I. Malik and E. Coady, 'Measurement of pulse wave velocity: Site matters,' *Journal of Hypertension*, vol. 25, no. 2, pp. 383–389, 2007, ISSN: 02636352. DOI: 10.1097/HJH.0B013E3280115BEA. [Online]. Available: https://journals.lww.com/jhypertension/fulltext/2007/02000/measurement_of_pulse_wave_velocity__site_matters.18.aspx.

[21] M. Zheng, Y. Huo, X. Wang and X. Xu, 'A prospective study on pulse wave velocity (PWV) and response to anti-hypertensive treatments: PWV determines BP control,' *International Journal of Cardiology*, vol. 178, pp. 226–231, Jan. 2015, ISSN: 0167-5273. DOI: 10.1016/J.IJCARD.2014.10.049. [Online]. Available: https://www.sciencedirect.com/science/article/abs/pii/S016752731401986X.

[22] M. Fasshauer, J. T. Kowallick, A. Joseph and C. Unterberg-Buchwald, 'Pulse wave velocity in real-time cardiac magnetic resonance,' *Journal of Cardiovascular Magnetic Resonance*, vol. 16, no. 1, p. 382, Jan. 2014, ISSN: 10976647. DOI: 10.1186/1532-429X-16-S1-P382/METRICS. [Online]. Available: https://jcmr-online.biomedcentral.com/articles/10.1186/1532-429X-16-S1-P382.

[23] N. Laban, R. Dawood and S. Y. Kuang, 'From compliance to moduli: clarifying basic mechanical properties of biological tissues,' *Advances in Physiology Education*, vol. 49, no. 3, pp. 651–658, 2025, ISSN: 15221229. DOI: 10.1152/ADVAN.00032.2025. [Online]. Available: /doi/pdf/10.1152/advan.00032.2025?download=true.

[24] P. Skacel and J. Bursa, 'Poisson's ratio of arterial wall – Inconsistency of constitutive models with experimental data,' *Journal of the Mechanical Behavior of Biomedical Materials*, vol. 54, pp. 316–327, Feb. 2016, ISSN: 1751-6161. DOI: 10.1016/J.JMBBM.2015.09.029. [Online]. Available: https://www.sciencedirect.com/science/article/abs/pii/S1751616115003665?via%3Dihub.

[25] D. J. Korteweg, 'Über die Fortpflanzungsgeschwindigkeit des Schalles in elastischen Röhren,' *Annalen der Physik*, vol. 241, no. 12, pp. 525–542, 1878, ISSN: 15213889. DOI: 10.1002/ANDP.18782411206. [Online]. Available: https://zenodo.org/records/1423762.

[26] A. Isebree Moens, *Die Pulscurve*, German. Leiden: E. J. Brill, 1878. [Online]. Available: https://openlibrary.org/books/OL24363799M/Die_Pulscurve.

[27] D. Shahmirzadi, R. X. Li and E. E. Konofagou, 'Pulse-Wave Propagation in Straight-Geometry Vessels for Stiffness Estimation: Theory, Simulations, Phantoms and In Vitro Findings,' *Journal of Biomechanical Engineering*, vol. 134, no. 11, p. 1 145 021, 2012, ISSN: 01480731. DOI: 10.1115/1.4007747. [Online]. Available: https://pmc.ncbi.nlm.nih.gov/articles/PMC5413152/.

[28] A. Tijsseling and A. Anderson, 'A. Isebree Moens and D.J. Korteweg: on the speed of propagation of waves in elastic tubes,' Technische Universiteit Eindhoven, Eindhoven., Eindhoven, Tech. Rep., 2012. [Online]. Available: https://research.tue.nl/en/publications/a-isebree-moens-and-dj-korteweg-on-the-speed-of-propagation-of-wa.

[29] M. A. B. Kevin, F. King and J. Zhou, *Handbook of MRI pulse sequences*. A&C Black Publishers Ltd., 2004. DOI: 10.1016/B978-0-12-092861-3.X5000-6.

[30] F. Schick, 'Grundlagen der Magnetresonanztomographie,' *Der Radiologe*, vol. 45, pp. 69–88, 2005. DOI: 10.1007/s00117-004-1146-1. [Online]. Available: https://link.springer.com/article/10.1007/s00117-007-1509-5.

[31] S. Wundrak *et al.*, 'Golden ratio sparse MRI using tiny golden angles,' *Magnetic resonance in medicine*, vol. 75, no. 6, pp. 2372–2378, Jun. 2016, ISSN: 1522-2594. DOI: 10.1002/MRM.25831. [Online]. Available: https://pubmed.ncbi.nlm.nih.gov/26148753/.

[32] S. Wundrak, J. Paul, J. Ulrici, E. Hell and V. Rasche, 'A small surrogate for the golden angle in time-resolved radial MRI based on generalized fibonacci sequences,' *IEEE Transactions on Medical Imaging*, vol. 34, no. 6, pp. 1262–1269, Jun. 2015, ISSN: 1558254X. DOI: 10.1109/TMI.2014.2382572. [Online]. Available: https://www.researchgate.net/publication/269933239_A_Small_Surrogate_for_the_Golden_Angle_in_Time-Resolved_Radial_MRI_Based_on_Generalized_Fibonacci_Sequences.

[33] J. Lotz, C. Meier, A. Leppert and M. Galanski, 'Cardiovascular Flow Measurement with Phase-Contrast MR Imaging: Basic Facts and Implementation,' *Radiographics*, no. 22(3), pp. 651–671, May 2002. DOI: 10.1148/radiographics.22.3.g02ma11651.

[34] R. Chavan, N. Kamble, C. Kuthe and S. Sarnobat, 'On Mechanical Behavior and Characterization of Soft Tissues,' *Biomedical Engineering and Computational Biology*, vol. 15, p. 11 795 972 241 294 115, Jan. 2024, ISSN: 1179-5972. DOI: 10.1177/11795972241294115. [Online]. Available: https://pmc.ncbi.nlm.nih.gov/articles/PMC11531667/.

[35] R. Valente *et al.*, 'Experimental Protocols to Test Aortic Soft Tissues: A Systematic Review,' *Bioengineering*, vol. 11, no. 8, p. 745, Aug. 2024, ISSN: 23065354. DOI: 10.3390/BIOENGINEERING11080745. [Online]. Available: https://pmc.ncbi.nlm.nih.gov/articles/PMC11351783/.

[36] *The Potential for 3D Printing Synthetic Myocardium*, https://www.stratasys.com/en/resources/case-studies/medtronic-dap-myocardium/ (accessed 12-01-2026). [Online]. Available: https://www.stratasys.com/en/resources/case-studies/medtronic-dap-myocardium/.

[37] *Addion GmbH — Professionelle 3D Druck Dienstleistung - Tirol*, https://addion.at/ (accessed 26-02-2026). [Online]. Available: https://addion.at/.

[38] *Creality LD-002R*, https://www.creality3dofficial.com/de/products/ld-002r-lcd-resin-3d-printer?srsltid=AfmBOooztnVh6dS8Uu4iqf1zyXQS27EOUvZScaTdmavvD3dUNRxQvZWb (accessed 27-10-2025). [Online]. Available: https://www.creality3dofficial.com/de/products/ld-002r-lcd-resin-3d-printer?srsltid=AfmBOooztnVh6dS8Uu4iqf1zyXQS27EOUvZScaTdmavvD3dUNRxQvZWb.

[39] *BASF Ultracur3D® FL 300 Flexible Photopolymer Material*, https://forward-am.com/material-portfolio/ultracur3d-photopolymers/flexible-elastomeric-line /ultracur3d-fl-300/ (accessed 08-05-2025). [Online]. Available: https://forward-am.com/material-portfolio/ultracur3d-photopolymers/flexible-elastomeric-line/ultracur3d-fl-300/.

[40] J. Illi *et al.*, 'Mechanical testing and comparison of porcine tissue, silicones and 3D-printed materials for cardiovascular phantoms,' *Frontiers in Bioengineering and Biotechnology*, vol. 11, Dec. 2023, ISSN: 2296-4185. DOI: 10.3389/fbioe.2023.1274673. [Online]. Available: https://www.ncbi.nlm.nih.gov/pmc/articles/PMC10725245/%20files/383/Illi%20et%20al.%20-%202023%20-%20Mechanical%20testing%20and%20comparison%20of%20porcine%20tissu.pdf%20https://www.ncbi.nlm.nih.gov/pmc/articles/PMC10725245/.

[41] *Dragon Skin™ 20 Product Information — Smooth-On, Inc.* https://www.smooth-on.com/products/dragon-skin-20/ (accessed 25-02-2026). [Online]. Available: https://www.smooth-on.com/products/dragon-skin-20/.

[42] *Dragon Skin™ 30 Product Information — Smooth-On, Inc.* https://www.smooth-on.com/products/dragon-skin-30/?quicksearch (accessed 25-02-2026). [Online]. Available: https://www.smooth-on.com/products/dragon-skin-30/?quicksearch.

[43] *Autodesk Fusion 360*, https://www.autodesk.com/de/products/fusion-360/overview (accessed 27-10-2025). [Online]. Available: https://www.autodesk.com/de/products/fusion-360/overview.

[44] Y. Ishikawa, H. Nabae, G. Endo and K. Suzumori, 'In-vacuum silicone rubber forming process for soft robots,' *ROBOMECH Journal*, vol. 12, no. 1, pp. 1–13, Dec. 2025, ISSN: 21974225. DOI: 10.1186/S40648-025-00296-4/FIGURES/10. [Online]. Available: https://link.springer.com/articles/10.1186/s40648-025-00296-4%20https://link.springer.com/article/10.1186/s40648-025-00296-4.

[45] *Zentrifugalpumpe GAMPT MultiFlow*, https://www.gampt.de/product/zentrifugalpumpe-multiflow/ (accessed 17-08-2025). [Online]. Available: https://www.gampt.de/product/zentrifugalpumpe-multiflow/.

[46] *3D Basics Basic Resin*, https://3d-basics.com/de/Basic-Resin (accessed 27-10-2025). [Online]. Available: https://3d-basics.com/de/Basic-Resin.

[47] Manuel Hölzl, *Ultrasound Based Flow Measurement System Suitable for MRI-Environment*, Graz, 2025.

[48] *Siemens Syngo*, https://www.siemens-healthineers.com/at/digital-health-solutions/syngovia (accessed 27-10-2025). [Online]. Available: https://www.siemens-healthineers.com/at/digital-health-solutions/syngovia.

[49] *Siemens MAGNETOM Vida*, https://www.siemens-healthineers.com/at/magnetic-resonance-imaging/3t-mri-scanner/magnetom-vida (accessed 27-10-2025). [Online]. Available: https://www.siemens-healthineers.com/at/magnetic-resonance-imaging/3t-mri-scanner/magnetom-vida.